Fryer, P., Pearce, J. A., Stokking, L. B., et al., 1990
Proceedings of the Ocean Drilling Program, Initial Reports, Vol. 125

12. SITE 784[1]

Shipboard Scientific Party[2]

HOLE 784A

Date occupied: 26 March 1989

Date departed: 30 March 1989

Time on hole: 4 days, 8 hr, 30 min

Position: 30°54.49′N, 141°44.27′E

Bottom felt (rig floor; m; drill-pipe measurement): 4912.1

Distance between rig floor and sea level (m): 11.30

Water depth (drill-pipe measurement from sea level; m): 4900.8

Total depth (rig floor; m): 5337.40

Penetration (m): 425.30

Number of cores: 45

Total length of cored section (m): 425.30

Total core recovered (m): 218.28

Core recovery (%): 51.3

Oldest sediment cored:
Depth (mbsf): 425.3
Nature: sheared, phacoidal serpentine
Age: (?)

Hard rock:
Nature: clasts of metavolcanic, meta-volcaniclastic, or serpentinized ultramafic rocks

Principal results: Site 784 is located approximately 7 km southwest of Site 783 on the lowermost, western flank of the same seamount on the inner wall of the Izu-Bonin Trench. The one hole drilled (Hole 784A) penetrated 425.3 m with a recovery of 51.3%. The stratigraphic section is divided into two lithologic units. The upper 321 m of sedimentary Unit I is of late Pleistocene to middle Miocene age or older and is subdivided into a vitric clayey silt, glass-rich silty clay/claystone (Subunit IA), a vitric claystone (Subunit IB), and a mixed claystone and silt-sized serpentine mud (Subunit IC). The lower 104 m is a phacoidal sheared serpentine microbreccia (Unit II).

Sediments from Subunits IA and IB are typically laminated and contain abundant graded beds, which are structures indicative of current activity during sediment deposition. They contain a high volcanogenic component and numerous ash layers, but a small carbonate/microfossil component, because of deposition at or below the carbonate compensation depth (CCD). Subunit IC shows a clear interfingering of background pelagic sediments, derived from the volcanic areas to the west, and silt-sized serpentine from the topographic high to the east.

Most structures in the Unit I claystones are extensional and include sets of *en echelon* tension veinlets and microfaults, some of which are clearly associated with water-escape pipes. Unit II contains pebbly serpentines with convolute lamination, sheared and relatively unsheared, pebbly, silt-sized serpentines without convolute lamination, and serpentine microbreccias. The ultramafic clasts are of variably serpentinized, tectonized harzburgite, subordinate dunites, and a few metabasalts. The middle Miocene or older age provides further evidence that the seamount is an older feature than that drilled in the Mariana forearc.

Analyses of interstitial waters indicate a steady change in composition with depth within the claystone, followed by an abrupt change in behavior at the claystone/serpentine boundary. Below this boundary, the most abrupt changes are in pH, which increases to 9.6 in the serpentine, and silica, which decreases to less than 10 μmol/kg. Of the other species, alkalinity, sulfate, magnesium, and sodium all decrease, calcium increases, and chlorinity, bromide, and salinity show no major changes. These data provide evidence for ongoing serpentinization at the Torishima Forearc Seamount. Studies of physical properties show that the average bulk densities are 1.57 g/cm^3 in the sediments of Unit I and 2.19 g/cm^3 in the serpentine of Unit II. The average compressional-wave velocities in the sediments and serpentines are 1.66 and 3.08 km/s, respectively. Thermal conductivities average about 0.9 W/mK in the sediments and 1.74 W/mK in the serpentine. Preliminary interpretation of paleomagnetic data from sediments between 0 and 160 m below seafloor (mbsf) indicates that because the inclinations of most samples lie between +15° and 15°, there may have been significant translation between the middle Miocene and the Pliocene.

BACKGROUND AND SCIENTIFIC OBJECTIVES

The choice of site was based on seismic data collected during the survey of the seamount prior to occupation of Site 783 (see "Underway Geophysics" chapter, this volume), which indicated that an eastward-dipping fault plane underlies the west flank of the seamount. Site 784 was located over the fault trace at 30°54.49′N, 140°44.27′E, at a water depth of 4900.8 m (Fig. 1). This position is approximately 7 km south-southwest of Site 783. Site 784 was a second attempt to penetrate the seamount on the inner wall of the Izu-Bonin Trench in order to (1) determine the nature of the pelagic sediments in the outermost forearc region, (2) investigate the regional tectonic history of the ridge upon which the seamount is located, (3) establish the age and mode of emplacement of the seamount through a study of the possible interlayered pelagic sediments and serpentine flows, (4) study the structure and composition of the basement of the seamount, and (5) determine the composition of the interstitial waters in the sediments and in serpentinites that might be encountered in the hole. A further objective specific to Site 784 was to recover interfingered pelagic sediments and serpentine flows that might help constrain the age of emplacement of the seamount or at least indicate the age of movement on faults associated with its uplift.

The seamount drilled at this site was dredged in 1988 in three locations (Fig. 1), yielding a wide variety of sedimentary and igneous/metamorphic rocks (Kobayashi, 1989). Most of the samples dredged from the western flank near Site 784 were sedimentary rocks, although some pumice fragments and a few serpentinized rocks were retrieved.

OPERATIONS

Transit to Site 784 (Proposed Site BON-7)

Because the basement objective had not been reached at Site 783, a hole was attempted on the lowermost western flank of the seamount, approximately 4 nmi from Site 783. Site 784 was established at 0630UTC, 26 March 1989, by the deployment of a beacon.

---

[1] Fryer, P., Pearce, J. A., Stokking, L. B., et al., 1990. *Proc. ODP, Init. Repts.*, 125: College Station, TX (Ocean Drilling Program).

[2] Shipboard Scientific Party is as given in the list of participants preceding the contents.

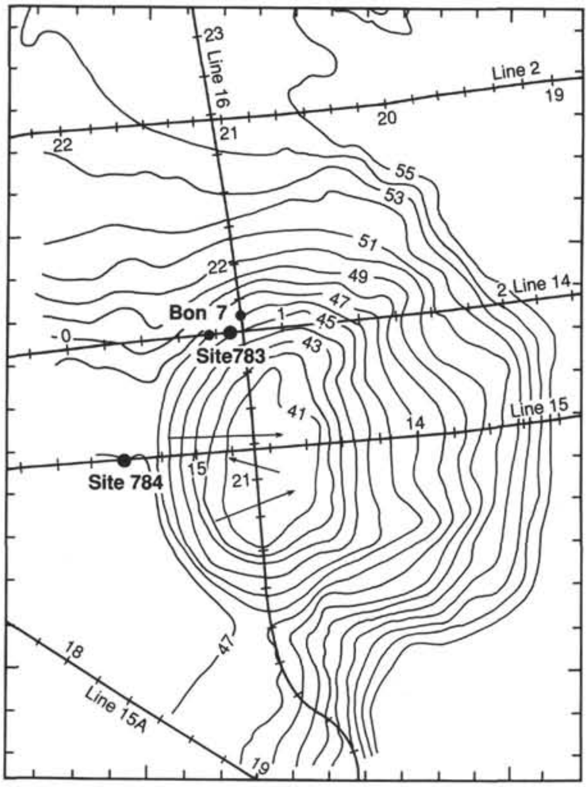

Figure 1. Bathymetry of the seamount at 31°N on the inner wall of the Izu-Bonin Trench. Arrows indicate the direction of the dredges taken on this seamount in 1988 (Kobayashi, 1989). Contour interval = 100 m.

Hole 784A

The trip back to the seafloor began at 0700UTC, and Hole 784A was spudded at 0830UTC, 26 March. From the first rotary core barrel (RCB) core we recovered 1.4 m of core and established the mud line at 4900.8 m below sea level (mbsl).

During preparations for logging, the bit failed to release several times. A core barrel was run in the hole to check for bit release, but became stuck at 21 mbsf. After retrieval of the core barrel, the drill string was tripped out of the hole. Five joints of drill string had bent, six stands above the bottom-hole assembly (BHA).

The RCB was deployed 45 times to a final depth of 425.3 mbsf, during which time we recovered 218.3 m of core for a recovery rate of 51.3% (Table 1). Site 784 officially ended at 0900UTC, 31 March, when the BHA was back on board and the vessel was under way for Site 785 (proposed Site BON-6A).

Table 1. Coring summary for Site 784.

Core no.	Date (March 1989)	Time (UTC)	Depth (mbsf)	Length cored (m)	Length recovered (m)	Recovery (%)
125-784A-						
1R	26	1010	0.0–1.4	1.4	1.40	100.0
2R	26	1210	1.4–10.9	9.5	0.20	2.1
3R	26	1345	10.9–20.4	9.5	5.13	54.0
4R	26	1455	20.4–29.9	9.5	5.43	57.1
5R	26	1820	29.9–39.5	9.6	0.00	0.0
6R	26	1930	39.5–49.1	9.6	8.48	88.3
7R	26	2130	49.1–58.8	9.7	4.30	44.3
8R	26	2215	58.8–68.5	9.7	7.94	81.8
9R	26	2330	68.5–78.1	9.6	6.93	72.2
10R	27	0045	78.1–87.8	9.7	5.86	60.4
11R	27	0200	87.8–97.4	9.6	0.20	2.1
12R	27	0300	97.4–107.1	9.7	2.62	27.0
13R	27	0530	107.1–116.7	9.6	0.78	8.1
14R	27	0700	116.7–126.4	9.7	7.18	74.0
15R	27	0800	126.4–136.0	9.6	9.85	102.0
16R	27	0910	136.0–145.6	9.6	9.82	102.0
17R	27	1200	145.6–155.3	9.7	7.52	77.5
18R	27	1300	155.3–165.0	9.7	9.85	101.0
19R	27	1425	165.0–174.7	9.7	3.29	33.9
20R	27	1525	174.7–184.4	9.7	7.68	79.2
21R	27	1640	184.4–194.0	9.6	8.36	87.1
22R	27	1800	194.0–203.6	9.6	8.67	90.3
23R	27	1915	203.6–213.2	9.6	3.86	40.2
24R	27	2025	213.2–222.9	9.7	9.51	98.0
25R	27	2145	222.9–232.5	9.6	1.19	12.4
26R	27	2300	232.5–242.1	9.6	4.23	44.0
27R	28	0015	242.1–251.8	9.7	7.66	78.9
28R	28	0130	251.8–261.4	9.6	3.60	37.5
29R	28	0245	261.4–271.1	9.7	9.82	101.0
30R	28	0345	271.1–280.8	9.7	6.85	70.6
31R	28	0445	280.8–290.4	9.6	4.43	46.1
32R	28	0545	290.4–300.0	9.6	9.64	100.0
33R	28	0700	300.0–309.7	9.7	5.42	55.9
34R	28	0800	309.7–319.3	9.6	3.31	34.5
35R	28	1145	319.3–329.0	9.7	2.59	26.7
36R	28	1500	329.0–338.7	9.7	1.22	12.6
37R	28	1900	338.7–348.3	9.6	2.26	23.5
38R	28	2330	348.3–357.9	9.6	2.66	27.7
39R	29	0600	357.9–367.5	9.6	2.81	29.3
40R	29	1020	367.5–377.3	9.8	2.76	28.1
41R	29	1320	377.3–386.9	9.6	2.57	26.8
42R	29	1720	386.9–396.6	9.7	2.44	25.1
43R	29	2330	396.6–406.3	9.7	3.90	40.2
44R	30	0400	406.3–415.6	9.3	0.97	10.4
45R	30	0800	415.6–425.3	9.7	3.09	31.8
Coring totals				425.3	218.28	51.3

LITHOSTRATIGRAPHY

The stratigraphic section recovered at Site 784 is divided into two lithologic units (Table 2). Lithologic Unit I consists of ash layers, feldspar- and glass-rich clayey silt, glass-rich silty clay/claystone, vitric claystone, claystone, and silt-sized serpentine and is divided into three subunits. Lithologic Unit II is composed of a serpentine microbreccia that is phacoidal and sheared and also exhibits vertical, convolute bedding.

Table 2. Lithologic units recovered at Site 784.

Lithologic unit	Cores	Depth (mbsf)	Dominant lithology	Stratigraphic age
IA	784A-1R-1, 0 cm, to 784A-14R-CC	0.0–126.4	Feldspar- and glass-rich clayey silt, glass-rich silty clay/ claystone	upper Pleistocene to lower Pliocene(?)
IB	784A-15R-1, 0 cm, to 784A-33R-2, 120 cm	126.4–302.7	Vitric claystone	lower Pliocene(?) to middle Miocene
IC	784A-33R-2, 120 cm, to 784A-35R-2, 34 cm	302.7–321.1	Claystone and silt-sized serpentine	?
II	784A-35R-2, 34 cm, to 784A-45R-CC	321.1–425.3	Sheared, phacoidal serpentine microbreccia with vertical convolute bedding	?

Table 3. Volcanic ash layers at Site 784.

Core, section, interval (cm)	Depth of top of section (mbsf)	True depth (mbsf)	Volcanic ash layer
125-784A-			
2R-1, 0–3	1.4	1.40–1.43	1
2R-1, 5–6	1.4	1.45–1.46	2
2R-1, 12–16	1.4	1.52–1.56	3
3R-3, 50–52	13.9	14.40–14.42	4
3R-3, 119–120	13.9	15.09–15.20	5
4R-2, 55–57	21.9	22.65–22.67	6
4R-3, 1–2	23.4	23.41–23.42	7
6R-1, 34	39.5	39.84	8
6R-2, 65–68	41	41.65–41.68	9
6R-2, 72–73	41	41.72–41.73	10
6R-3, 70	42.5	43.2	11
6R-3, 91–94	42.5	43.41–43.44	12
6R-4, 58	44	44.58	13
6R-5, 71–72	45.5	46.21–46.22	14
6R-5, 97–98	45.5	46.47–46.48	15
6R-6, 73.5–74.0	47	47.735–47.740	16
7R-1, 34–37	49.1	49.44–49.47	17
7R-2, 31–35	50.6	50.91–50.95	18
7R-2, 70–74	50.6	51.30–51.34	19
7R-3, 27–31	52.1	52.37–52.41	20
7R-3, 68–76	52.1	52.78–52.86	21
8R-1, 28–30	58.8	59.08–59.1	22
8R-1, 55–56	58.8	59.35–59.36	23
8R-2, 70–71	60.3	61.0–61.01	24
8R-3, 10–17	61.8	61.90–61.97	25
8R-3, 91	61.8	62.71	26
8R-4, 30–33	63.3	63.60–63.63	27
8R-4, 90–91	63.3	64.20–64.21	28
8R-4, 120–121	63.3	64.50–64.51	29
8R-5, 36–37	64.8	65.16–65.17	30
8R-5, 59–62	64.8	65.39–65.42	31
8R-5, 126–127	64.8	66.06–66.07	32
8R-5, 139.5–140.5	64.8	66.195–66.205	33
9R-1, 20–24	68.5	68.70–68.74	34
9R-1, 26.5–28.5	68.5	68.765–68.785	35
9R-1, 68–70	68.5	69.18–69.20	36
10R-3, 28–30	81.1	81.38–81.40	37
12R-2, 63–65	98.9	99.53–99.55	38
14R-2, 0–21	118.2	118.20–118.41	39
15R-1, 67–69	126.4	127.07–127.09	40
15R-2, 36–38	127.9	128.26–128.28	41
15R-2, 39	127.9	128.29	42
15R-2, 48–50	127.9	128.38–128.40	43

Table 3 (continued).

Core, section, interval (cm)	Depth of top of section (mbsf)	True depth (mbsf)	Volcanic ash layer
15R-2, 62–63	127.9	128.52–128.53	44
15R-2, 63–66	127.9	128.53–128.56	45
15R-4, 56–60	130.9	131.46–131.50	46
15R-5, 5–20	132.4	132.45–132.60	47
15R-5, 86–96	132.4	133.26–133.36	48
15R-6, 128–136	133.9	135.18–135.26	49
16R-2, 53–68	137.5	138.03–138.18	50
16R-3, 33	139	139.33	51
16R-3, 98–106	139	139.98–140.06	52
16R-4, 44–46	140	140.44–140.46	53
16R-4, 103–104	140	141.03–141.04	54
17R-2, 102–114	147.1	148.12–148.24	55
17R-3, 80–81	148.6	149.40–149.41	56
17R-3, 118–123	148.6	149.78–149.83	57
17R-3, 143–150	148.6	150.03–150.10	58
17R-4, 38–39	150.1	150.48–150.49	59
17R-4, 112–115	150.1	151.22–151.25	60
17R-4, 139–140	150.1	151.49–151.50	61
17R-5, 59–62	151.6	152.19–152.22	62
18R-2, 32–33	156.8	157.12–157.13	63
18R-2, 100–101	156.8	157.8–157.81	64
20R-1, 18–19	174.7	174.88–174.89	65
20R-1, 31–32	174.7	175.01–175.02	66
20R-1, 95–96	174.7	175.65–175.66	67
20R-1, 110	174.7	175.8	68
20R-1, 126–127	174.7	175.96–175.97	69
20R-1, 142–144	174.7	176.12–176.14	70
20R-2, 9–10	176.2	176.29–176.30	71
20R-2, 16–17	176.2	176.36–176.37	72
20R-2, 40–41	176.2	176.60–176.61	73
20R-3, 65–70	177.7	178.35–178.40	74
20R-4, 13–17	179.2	179.33–179.37	75
21R-3, 68	187.4	188.08	76
21R-3, 77–80	187.4	188.17–188.20	77
21R-3, 139–140	187.4	188.79–188.80	78
21R-4, 78–84	188.9	189.68–189.74	79
22R-3, 88–95	197	197.88–197.95	80
24R-3, 121–123	216.2	217.41–217.43	81
24R-4, 47–50	217.7	218.17–218.20	82
27R-5, 31–35	248.1	248.41–248.45	83
28R-1, 94–96	251.8	252.74–252.76	84
29R-6, 78–80	268.9	269.68–269.70	85
31R-2, 8–11	282.3	282.38–282.41	86

Unit I

Sections 125-784A-1R-1, 0.0 cm, to 125-784A-35R-2, 34 cm; depth, 0.0–321.1 mbsf.
Age: late Pleistocene to ?

Unit I extends from the sediment/water interface to 321.1 mbsf. The gradational transition from Subunit IA to Subunit IB is based on color change, volcanic input, and extent of bioturbation. The upper part of lithologic Unit I (Subunits IA and IB) is composed primarily of claystone with varying amounts of volcanic glass and ash layers. The general trend of the volcanic input increases downhole, as can be seen in the detailed listing of ash layers in Table 3. Lithologic Subunit IC is distinct from the upper part of lithologic Unit I; this subunit contains nearly glass-free claystone with interbedded silt-sized serpentine.

Subunit IA

Sections 125-784A-1R-1, 0.0 cm, to 125-784A-14R-CC; depth, 0.0–126.4 mbsf.
Age: late Pleistocene to early Pliocene(?).

Lithologic Subunit IA contains ash layers, but is composed predominantly of light and dark gray (2.5Y 6/0 and 2.5Y 4/0), feldspar- and glass-rich clayey silt and glass-rich, silty clay/claystone scattered with brown (10YR 5/3), subangular to subrounded pumice fragments, 0.5 to 4 cm in diameter. Intervals of dark greenish gray (10Y 5/2), vitric silty clay that begin to appear in the light gray sediment of Core 125-784A-6R predominate by the top of lithologic Subunit IB. Lithologic Subunit IA has varying amounts of silt-sized detritus within the claystone, usually representing a volcanic influx. The main components of this detritus are glass (21%–53%), feldspar (8%–22%), pyroxene (0%–7%), epidote (0%–3%), amphibole (0%–2%), and chlorite (rarely present, and only in trace amounts). A trace to 10% of zeolite present in Cores 125-784A-2R through 125-784A-4R and 125-784A-6R through 125-784A-9R is interpreted as an alteration product of volcanic glass. Cores 125-784A-2R through 125-784A-4R, in the uppermost part of this subunit, contain some sand-sized quartz, which on the basis of grain size can be interpreted as terrigenous detritus, rather than an aeolian contribution. Serpentine (less than 10%) was observed in Cores 125-784A-3R, 125-784A-4R, 125-784A-6R, 125-784A-8R, 125-784A-12R, and 125-784A-14R.

The majority of the ash layers in Subunit IA are black (N 4/0 to N 2/0) graded beds with sharp basal contacts, except where drilling disturbance is severe. The different colors of the ash result from a slight variation in the feldspar and opaque mineral contribution to the sediment. The ash from this subunit is composed of volcanic glass (64%–90%) and feldspar (3%–20%), sporadic amounts of pyroxene (as much as 10%), opaque minerals (as much as 10%), chlorite (trace amounts), and clays (as much as 20%). There are also a few layers of vitric sands and silts with large admixtures of clay (30%–40%) that are interpreted as reworked ash.

In addition to the ash beds with normal grading, the prevalent sedimentary structures in Subunit IA are laminations. Intervals with laminations are present downhole from Core 125-784A-8R, and the number of intervals increases with depth to the base of this subunit, indicating current activity during deposition of the sediment. At the base of this subunit, in Section 125-784A-14R-CC, is a 4.5-cm-thick graded bed with a 0.5-cm-thick base of very pale brown (10YR 8/3) rhodochrosite (confirmed by X-ray diffraction) silt.

The only tectonic structures observed in Subunit IA are *en echelon* tension gashes in Section 125-784A-6R-5, 50–60 cm. For detailed discussion of this feature, see "Structural Studies" section (this chapter).

Biologic sedimentary structures are rare throughout Subunit IA. The background sediment of the subunit contains only a small biogenic contribution of radiolarians (as much as 10%), diatoms (as much as 10%), spicules (as much as 5%), silicoflagellates (rarely present, at trace amounts to 10%), and nannofossils (found only in Core 125-784A-8R as 2% of a reworked ash deposit). Nannofossils are not typically preserved in this environment beneath the CCD unless they were rapidly deposited from shallower depths and rapidly buried in the redeposited ash layer.

Diatoms were used to determine the biostratigraphic age of Subunit IA. Sample 125-784A-1R-1, 10–20 cm, near the top of the first core, provides a stratigraphic age of late Pleistocene for the uppermost sediment in Unit I. Section 125-784A-12R-CC, near the base of the unit, has a diatom biostratigraphic age of early Pliocene; the age of the oldest strata in Subunit IA is not well constrained, but is at least early Pliocene.

Subunit IB

Sections 125-784A-15R-1, 0.0 cm, to 125-784A-33R-2, 120 cm; depth, 126.4–302.7 mbsf.
Age: early Pliocene(?) to middle Miocene.

Lithologic Subunit IB also contains ash layers, but is composed predominantly of dark gray (5GY 4/1), glass-rich silty claystone. This sediment is sufficiently indurated from burial diagenesis to be classified as a claystone. Subunit IB has varying amounts of silt-sized detritus, probably representing a volcanic influx. Glass (15%–52%) is always present; other minerals observed are feldspar (as much as 15%), pyroxene (as much as 3%), chlorite (as much as 1%), and amphibole (as much as trace amounts). Zeolites were found only in Cores 125-784A-16R and 125-784A-17R, and quartz is present in this subunit in Cores 125-784A-20R through 125-784A-22R and 125-784A-24R in amounts less than 2%.

The ash layers of Subunit IB have sharp basal contacts and are composed of volcanic glass (68%–98%) and feldspar (2%–17%), sporadic amounts of pyroxene (as much as 7%), opaque minerals (as much as 10%), chlorite (as much as 1%), and clays (as much as 15%). Some of the ash layers contain both clinopyroxene and orthopyroxene.

Serpentine was also observed in some of the vitric claystones from Cores 125-784A-16R, 125-784A-23R, 125-784A-24R, 125-784A-32R, and 125-784A-33R, in amounts of less than 5%. An exception is in Section 125-784A-16R-6, 51–56 cm, where the core is cut by a series of greenish gray (5G 4/2) veins(?) composed of 20% serpentine, 10% opaque minerals, 70% clays, and trace amounts of feldspar and pyroxene.

Sedimentary structures in this subunit include abundant graded beds, parallel laminations, inclined laminations, micro-cross laminations (Samples 125-784A-15R-2, 36–38 cm, 125-784A-15R-2, 48–50 cm, and 125-784A-16R-3, 33–34 cm), a complete Bouma sequence (Section 125-784A-18R-1, 96–125 cm), and wavy laminations (Section 125-784A-23R-3, 40–46 cm). These structures indicate current activity during deposition of the sediment. Extensive bioturbation is also a characteristic feature of this subunit.

Other physical structures observed in this subunit are synsedimentary microfaults (Sections 125-784A-18R-2, 100–112 cm, 125-784A-19R-1, 60–68 cm, 125-784A-19R-1, 75–77 cm, 125-784A-27R-5, 12–24 cm, and 125-784A-32R-5, 12–18 cm), water-escape structures (Section 125-784A-32R-3, 0–60 cm), and tension gashes (Sections 125-784A-32R-4, 125-784A-32R-5, and 125-784A-33R-1, 28–32 cm). For a detailed discussion of these features, see the "Structural Studies" section (this chapter).

Subunit IB contains a small siliceous biogenic contribution composed of spicules (as much as 10%), radiolarians (as much as 10%), diatoms (as much as 5%), and silicoflagellates (rarely present, in trace amounts). Calcareous biogenic components are only present in Core 125-784A-31R as a trace amount of foraminifers and 5% nannofossils.

The stratigraphic age of this subunit is not well constrained. A diatom biostratigraphic age of late Miocene was obtained from core-catcher Samples 125-784A-21R and 125-784A-22R, and a middle Miocene age from core-catcher Samples 125-784A-26R, 125-784A-27R, and 125-784A-31R. Using this information and the constraint imposed by the age determination for the base of the overlying subunit, Subunit IB must be early Pliocene to at least middle Miocene.

Subunit IC

Sections 125-784A-33R-2, 120 cm, to 125-784A-35R-2, 34 cm; depth, 302.7–321.1 mbsf.

Lithologic Subunit IC is composed of intercalated grayish brown to olive brown (2.5Y 5/2 to 2.5Y 4/4) claystone and dark blue gray (5B 4/1) silt-sized serpentine. The claystone is devoid of any sedimentary structures in Core 125-784A-32R, with the exception of irregular, pale green (5G 6/2) areas (millimeter to centimeter size), some of which surround small white (2.5Y 8/0) preexisting(?) millimeter-sized clasts, and of irregular horizontal zones composed of pale green vitric-bearing claystone. The background claystone is composed of clay (90%–100%), serpentine (trace–2%), feldspar (1%–3%), glass (1%–7%), and a trace of pyroxene and amphibole. The silt-sized serpentine is typically interlayered with the claystone, with the exception of a different structure in the serpentine interval from 91 to 136 cm in Section 125-784A-35R-1. From 91 to 121 cm is a serpentine breccia composed of a dark gray (N 4/0), 5 × 6 cm rounded clast with a faint phacoidal texture and dark greenish gray (5BG 4/1), millimeter-sized angular grains. The matrix is silt-sized serpentine with layers of the following colors: bluish gray (5B 5/1) at 91–117 cm, yellowish brown (10YR 5/6) at 117–118 cm, and greenish gray (5GY 6/1) at 118–121. From 121 to 136 cm in Section 125-784A-35R-1, rounded bluish gray (5B 5/1), angular greenish gray (5GY 6/1), and rounded yellowish brown (10YR 5/6) millimeter-sized clasts are scattered through a finer-scale variegated (same matrix colors as noted for the interval from 91 to 121 cm) matrix with a sigmoidal pattern. Subunit IC contains no biogenic contribution and no stratigraphic age has therefore been determined.

The change from clay to claystone from Subunit IA to Subunit IB is typical of burial diagenesis. Lithologic Subunit IA differs from Subunit IB in color and the degree of bioturbation and probably correlates with lithologic Unit I at Site 783 on the northern flank of the seamount because the ages, lithologies, and thicknesses at the two sites are similar. Subunit IB at Site 784 may correlate with lithologic Subunit IB at Site 782 in the forearc basin because of the similarity in age and ash content, but the lithologies differ. The sediment in Subunit IB at this site has a depleted carbonate contribution because of its proximity to the CCD. The *in-situ* pelagic sediments and the silt-sized serpentine that has flowed down from the adjacent topographic high interfinger at Site 784 in Subunit IC, the lowermost part of Unit I.

Unit II

Sections 125-784A-35R-2, 34 cm, to 125-784A-45R-CC; depth, 321.1–425.3 mbsf.

The contact between lithologic Units I and II is represented by an abrupt change to grayish green (5G 5/2) and bluish gray (5B 5/1) sheared, phacoidal serpentine microbreccia withvertical, convolute bedding. A microbreccia containing blocks of serpentinized harzburgite in a matrix of sheared, phacoidal serpentine first occurs in Core 125-784A-36R and continues throughout the remainder of the unit. In the lowermost part of Unit II is a silt-sized serpentine (bearing apatite in Core 125-784A-44R) associated with the sheared, phacoidal serpentine microbreccia and the blocks of harzburgite.

The presence of Pleistocene nannofossils and siderite (rhodochrosite?) siltstone indicates downhole contamination at the tops of Cores 125-784A-36R through 125-784A-39R and 125-784A-43R. No fossils were found within the serpentine microbreccia; the age of these strata is, therefore, unknown.

Lithologic Unit II is probably either locally derived from the adjacent topographic high or represents the underlying "acoustic basement" at this site. This unit correlates with lithologic Unit II at Site 783 on the northern flank of the seamount.

BIOSTRATIGRAPHY

Evidence from calcareous nannofossils and diatoms in the cores from Site 784 shows that the sedimentary interval from Samples 125-784A-1R-1, 10–20 cm, to 125-784A-31R-CC ranges in age from late Pleistocene to middle Miocene. No ages could be assigned to the remaining sedimentary section in Cores 125-784A-32R to 125-784A-42R.

The strong dissolution of the calcareous plankton assemblages from Site 784 suggests that deposition of the sedimentary interval probably took place at or below the CCD.

The biostratigraphic results of Site 784 are summarized in Figure 2.

Calcareous Nannofossils

Rare, poorly preserved calcareous nannofossil assemblages were found in Samples 125-784A-2R-CC, 125-784A-6R-CC, and 125-784A-8R-3, 15 cm. The presence of *Gephyrocapsa oceanica*, *Gephyrocapsa caribbeanica*, and *Pseudoemiliania lacunosa* confines Samples 125-784A-2R-CC and 125-784A-6R-CC to the middle/early Pleistocene (Zone CN14a). Sample 125-784A-8R-3, 15 cm, contains a late Pliocene (Zone CN12) assemblage of *Discoaster brouweri*, *P. lacunosa*, *Calcidiscus macintyrei*, and *Helicosphaera sellii*. The low abundance and poor preservation are probably the result of deposition at or below the CCD, as shown by the strong etching of the remaining nannofossil assemblages.

Foraminifers

Except for Sample 125-784A-2R-CC, in which a single specimen of *Globigerina* sp. was found, all of the samples examined, from Samples 125-784A-1R-1, 10–20 cm, to 125-784A-42R-CC, are barren of planktonic and benthic foraminifers. This is again most likely the result of deposition below the CCD.

Diatoms

Diatoms are poorly to well preserved and are sparse to abundant in Hole 784A. It was possible to date the sedimentary interval as ranging from late Pleistocene to at least middle Miocene. The interval below Core 125-784A-31R-CC is devoid of diatoms.

Sample 125-784A-1R-1, 10–20 cm, is assigned to the late Pleistocene *Pseudoeunotia doliolus* Zone by the appearance of *P. doliolus* and the absence of *Nitzschia reinholdii*.

Nitzschia reinholdii is present in Sample 125-784A-2R-CC; this sample is, therefore, early Pleistocene (*N. reinholdii* Zone).

No zonal markers were found in Samples 125-784A-3R-CC through 125-784A-6R-CC. The Pliocene/Pleistocene boundary can be assumed to be in this interval, as *Rhizosolenia praebergonii* is present in Samples 125-784A-7R-CC and 125-784A-8R-CC, which assigns these samples to the late Pliocene *R. praebergonii* Zone. Both samples have abundant and well-preserved assemblages.

The early Pliocene marker *Nitzschia jouseae* is present in Samples 125-784A-10R-CC and 125-784-12R-CC.

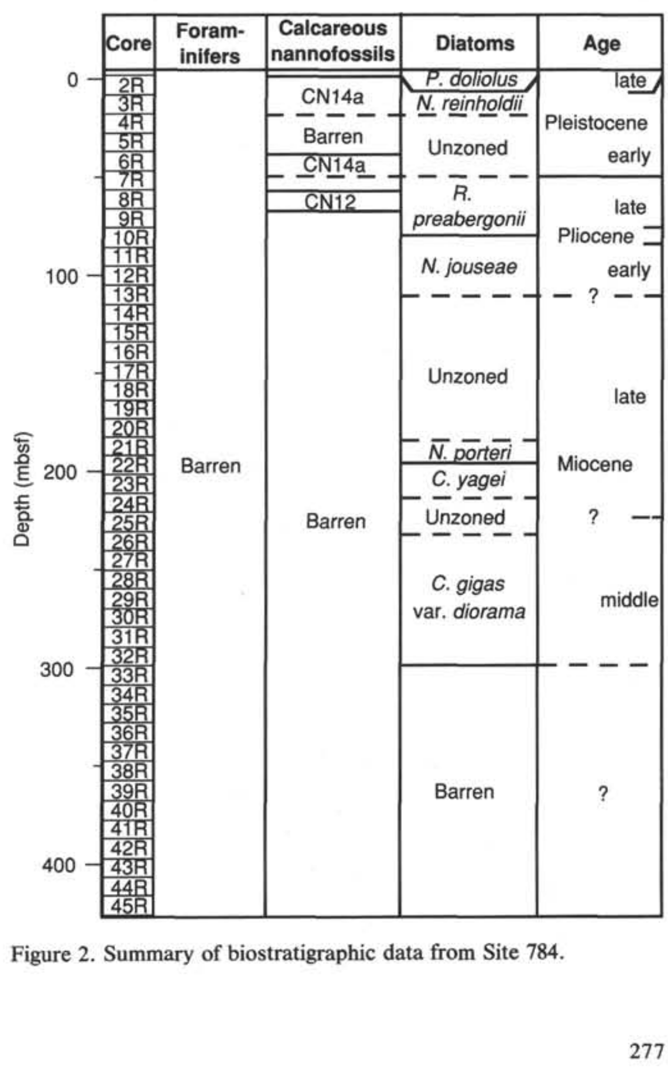

Figure 2. Summary of biostratigraphic data from Site 784.

Samples 125-784A-13R-CC through 125-784A-20R-CC have only traces or rare abundances of diatoms in which no zonal markers were found.

Thalassiosira burckliana is present in Sample 125-784A-21R-CC and *Coscinodiscus yabei* was recorded in Sample 125-784A-22R-CC, which assigns these samples to the late Miocene. Both samples have common and moderately preserved assemblages.

Samples below 125-784A-22R-CC have only traces of diatoms. *Actinocyclus ingens* is present in Samples 125-784A-26R-CC through 125-784A-31R-CC, dating this interval as middle Miocene (*Coscinodiscus gigas* var. *diorama* Zone or older).

IGNEOUS AND METAMORPHIC PETROLOGY

The igneous and metamorphic rocks recovered at Site 784 are variably serpentinized and tectonized ultramafic rocks (harzburgite 80%–90%, dunite 10%–20%) together with weakly metamorphosed volcanic (metabasalt and meta-volcaniclastic) rocks. The ultramafic clasts reach a maximum recovered thickness of about 1.5 m (Section 125-784A-43R-2) and are enclosed in a highly sheared and pulverized serpentine matrix (Fig. 3) that is described in the "Structural Studies" section (this chapter). Contact relationships between the ultramafic and sedimentary rocks are ambiguous. The volcanic clasts are 1 to 5 cm in diameter and show a subangular to subrounded shape. They form clasts of isolated fragments and inclusions in the serpentine matrix.

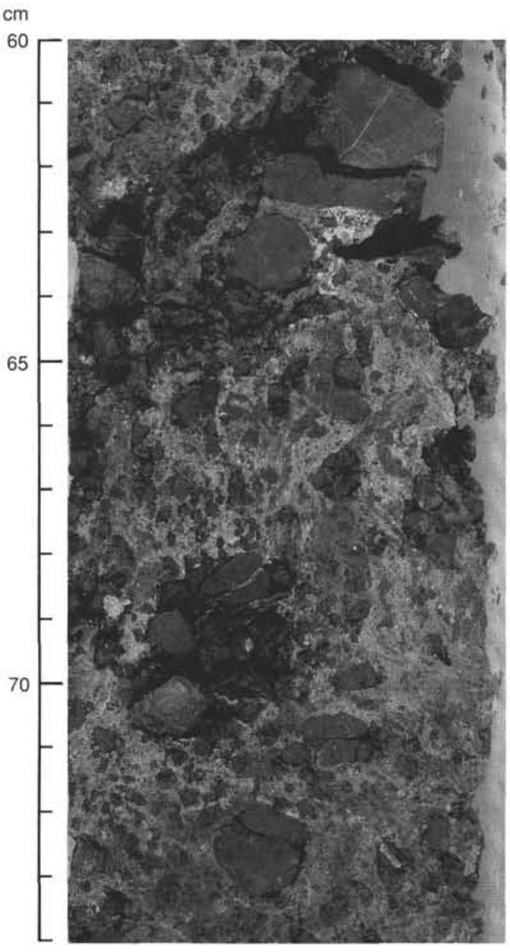

Figure 3. Ultramafic clasts enclosed in a highly sheared and pulverized serpentine matrix (Section 125-784A-43R-2, 60–74 cm).

Ultramafic Rocks

Serpentinized and Weakly Tectonized Harzburgites

The harzburgites are massive and vary from dark greenish-gray (5BG 4/1), where relatively fresh, to black (7.5YR 2/0), where serpentinized (e.g., Sections 125-784A-38R-2, 85–94 cm, and 125-784A-36R-1, 94–107 cm; Figs. 4 and 5, respectively). The primary mineralogy of these rocks is olivine (65%–90%), orthopyroxene (10%–30%), clinopyroxene (trace–4%), and chromium-spinel (trace–2%). Clinopyroxene is present as blebs and anhedral crystals (<2 mm), typically closely related to orthopyroxene, and as exsolution lamellae (on 100) in orthopyroxene.

The harzburgites display weak deformation. Typically, orthopyroxene crystals are 1 to 5 mm in size and have morphologies that range from equant to asymmetric-elongate; the cleavage surfaces and extinction are wavy, kink-banding is not rare, and fine clinopyroxene exsolution lamellae on (100) are bent. Olivine crystals are 1 to 5 mm in size and have an anhedral shape. Kink-banding characterizes some olivine morphologies. Chromium-spinel crystals are subhedral to anhedral (0.05–1.5 mm in size) and dark red to reddish brown in thin section. Some of the elongate spinels define a lineation parallel to the elongate olivine and orthopyroxene (see "Structural Studies" section, this chapter).

The degree of serpentinization is extremely variable (60%–100%), with the olivine and orthopyroxene replaced by mesh-textured serpentine and bastite (which appear to be mostly chrysotile and/or lizardite), respectively. In the strongly serpentinized types, most of the chromium-spinel (translucent, shades of red) is replaced by magnetite (opaque). The harzburgites are cut by numerous veins of serpentine. Many of these veins show a polystage history of filling (Fig. 5). Typically, serpentinization has affected olivine the most, orthopyroxene less, and clinopyroxene and chromium-spinel the least at this site. Subhedral primary clinopyroxenes (<2 mm in length) were observed in some samples.

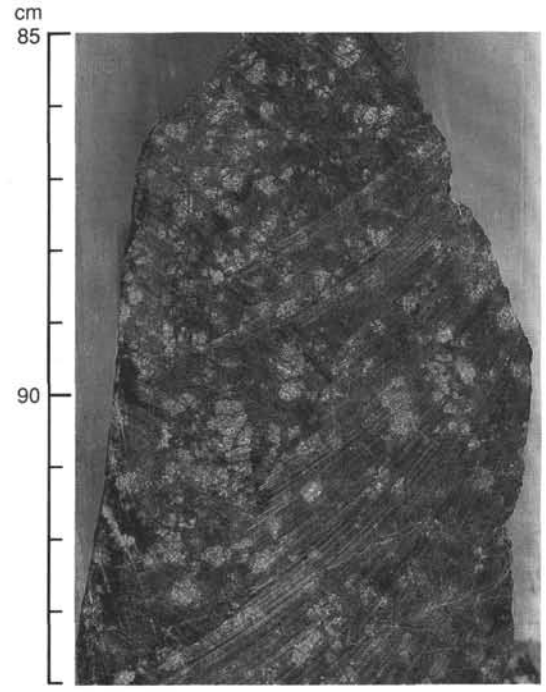

Figure 4. Relatively pyroxene-rich fresh harzburgite (Section 125-784A-38R-2, 85–94 cm).

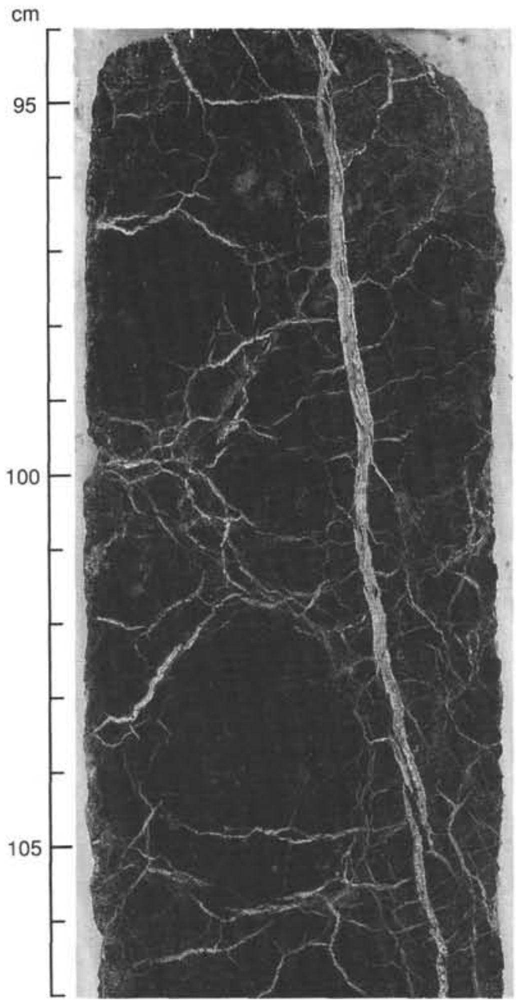

Figure 5. Intensively serpentinized harzburgite cut by numerous veins of serpentine (Section 125-784A-36R-1, 94–107 cm).

Serpentinized and Weakly Tectonized Dunites

The dunites are dark bluish gray (5B 4/1) to black (N 4/) and generally massive; some grade to harzburgite. The primary mineralogy consists of olivine (>95%), orthopyroxene (<5%), and spinel (trace–1%). Most of the dunites are extensively (99%–100%) serpentinized, show mesh textures and splays of chrysotile (and/or lizardite), and are cut by numerous serpentine-rich veins (Fig. 6). Asymmetric elongation of spinel is evidence of deformation. Other secondary minerals include magnetite (replacing chromium-spinel and in serpentine veins) and up to 10% clays (replacing serpentine).

Metavolcanic Rocks

Metabasalt

The several clasts of metabasalt that were recovered are 1 to 5 cm in diameter. Most are grayish green (5G 4/2–5G 5/2), and those containing abundant limonite are dark reddish brown (5YR 2.5/2). The metabasalts are composed of plagioclase, clinopyroxene, magnetite(?), and glass as primary phases and chlorite, sphene, dusty brownish clay, carbonate, pale green actinolite, and limonite as secondary phases. The primary igneous textures, such as intersertal and aphyric textures, are well preserved, but almost all primary minerals, except clinopyroxene and some plagioclase grains, are completely altered.

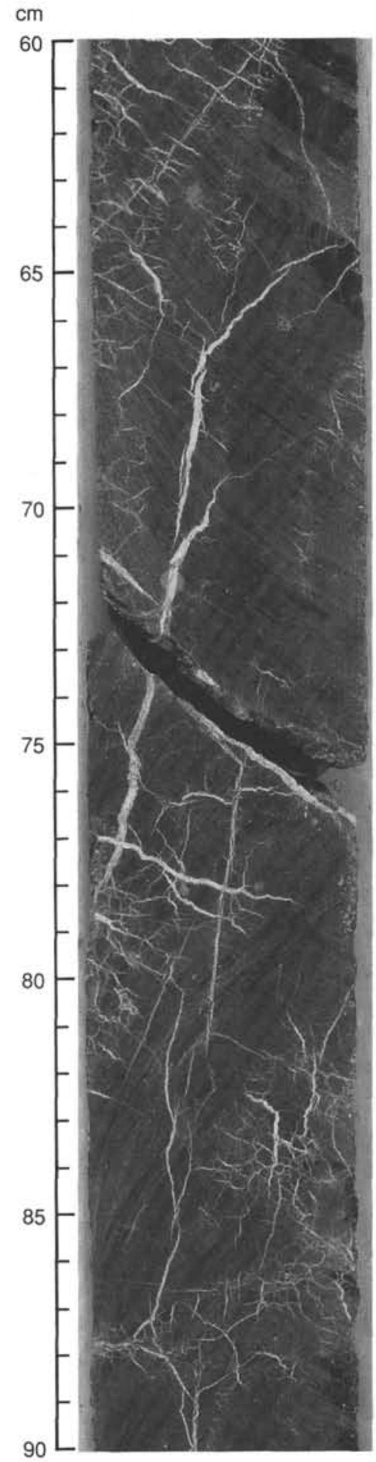

Figure 6. Intensively serpentinized dunite cut by numerous veins of serpentine (Section 125-784A-40R-2, 60–90 cm).

Meta-Volcaniclastic Rock

Only one meta-volcaniclastic rock clast was recovered. The rock is 5 cm in diameter, light greenish gray (5G 7/1), and medium- to fine-grained and consists of clinopyroxene as a relic mineral and prehnite, dusty brownish clay, carbonate, actinolite, and chlorite as secondary minerals. The rock contains abundant subangular to subrounded fragments of clinopyroxene within a fine-grained chlorite and clay matrix.

Most fragments of clinopyroxene have been altered to colorless actinolite. Calcite and chlorite veins (0.01–0.1 mm wide) run throughout the rock.

IGNEOUS AND METAMORPHIC GEOCHEMISTRY

Shipboard geochemical analyses of clasts enclosed in a highly sheared and pulverized serpentine matrix at Site 784 were performed for seven samples of serpentinized harzburgites, three samples of serpentinized dunites, and two matrix samples. Preparation and analytical techniques are given in the "Explanatory Notes" (this volume). Rock and thin-section descriptions are given in "Igneous and Metamorphic Petrology" section of this chapter. The geochemical data are listed in Tables 4 and 5.

Ultramafic Samples

Modal estimates of the original (pre-serpentinization) composition of ultramafic samples range from 65 to 93 modal% olivine, 10 to 30 modal% orthopyroxene, trace to 4 modal% clinopyroxene, and trace to 2 modal% spinel in the harzburgite samples and from 95 to 99 modal% olivine, <5 modal% orthopyroxene, and trace to 1 modal% spinel in the dunite samples. The degree of serpentinization of the samples varies from 60% to 100% for the harzburgites and from 99% to 100% for the dunites.

Major-Element Chemistry

Loss on ignition (LOI) for these samples ranges from 13.63 to 17.01 wt%, and, as for the samples from Sites 779 and 783, shows a positive correlation with the degree of serpentinization (Fig. 7A). (See "Igneous and Metamorphic Geochemistry" sections in the "Site 778" and "Site 779" chapters, this volume, and "Explanatory Notes" chapter for an explanation of LOI.) Although the ranges of major-element concentrations are similar in the dunite and harzburgite samples, some small differences exist. SiO_2 is slightly higher in the harzburgite samples (35.35–38.92 wt%) than in the dunite samples (33.01–34.17 wt%). Al_2O_3 is also slightly higher in the harzburgites (0.27–0.62 wt%) than in the dunites (0.01–0.20 wt%). Fe_2O_3 ranges from 7.13 to 8.94 wt% and CaO ranges from 0.06 to 0.55 wt% in both. MgO values in dunite samples (39.36–41.33 wt%) are slightly higher than in harzburgite samples (37.93–39.67 wt%). Magnesium number (Mg# = Mg/(Mg + Fe) × 100) is high in all rocks and ranges from 89.71 to 91.67. Na_2O, K_2O, and P_2O_5 were not detected in any of the samples. The general absence of clinopyroxene crystals and very low concentrations of Al_2O_3 and CaO (Fig. 7B) indicate that the rocks are residues from high degrees of partial melting. Concentrations of major-element oxides in ultramafic rocks from Site 784 are similar to those from ultramafic samples from Sites 778 through 780 and 783 (see the "Igneous and Metamorphic Geochemistry" sections in the respective site chapters).

Trace-Element Chemistry

Trace-element data are presented in Table 5. Compatible elements are high in all samples, as expected. Nickel ranges from 1991 to 2819 ppm and chromium from 1115 to 2585 ppm, with the exception of a single low value of 444 ppm in Sample 125-784A-40R-2, 41–43 cm. Chromium and nickel do not correlate with one another or with the degree of serpentinization. Niobium, zirconium, yttrium, rubidium, and titanium are all present in trace amounts or are below detection limits, with the exception of Sample 125-784A-45R-1, 98–100 cm, which contained a high value of 18 ppm for zirconium. Cerium and barium values range from below the detection limit (<10 ppm) to trace amounts and 12 ppm, respectively, although these values may result from analyt-

Table 4. Major-element data for serpentinized ultramafic rocks and matrix samples from Hole 784A.

Core, section: Interval (cm):	36R-1, 107–109	37R-1, 6–9	38R-1, 66–68	38R-2, 92–95	42R-1, 5–8	45R-1, 98–100	45R-2, 41–44	Average harzburgite	40R-2, 41–43	41R-2, 98–100	42R-1, 39–41	Average dunite	38R-2, 29–31	40R-1, 84–87	Average matrix
SiO_2	36.23	36.97	35.35	38.92	37.57	37.58	37.78	37.20	33.32	34.17	33.01	33.50	36.98	36.18	36.58
TiO_2	0.00	0.00	0.00	0.00	0.00	0.00	0.00	0.00	0.00	0.00	0.00	0.00	0.00	0.00	0.00
Al_2O_3	0.27	0.51	0.29	0.62	0.52	0.34	0.35	0.41	0.01	0.15	0.20	0.12	0.34	0.17	0.26
Fe_2O_3	7.44	7.54	7.21	7.13	7.49	7.24	7.14	7.31	7.92	8.94	8.90	8.59	6.62	7.17	6.90
MnO	0.12	0.16	0.13	0.13	0.11	0.11	0.11	0.12	0.11	0.12	0.13	0.12	0.08	0.09	0.09
MgO	38.85	38.30	39.15	37.93	39.28	39.63	39.67	38.97	41.33	39.36	40.31	40.33	39.86	40.55	40.21
CaO	0.06	0.41	0.07	0.58	0.55	0.46	0.54	0.38	0.14	0.14	0.14	0.14	0.08	0.17	0.13
Na_2O	0.00	0.00	0.00	0.00	0.00	0.00	0.00	0.00	0.00	0.00	0.00	0.00	0.00	0.00	0.00
K_2O	0.00	0.00	0.00	0.00	0.00	0.00	0.00	0.00	0.00	0.00	0.00	0.00	0.00	0.00	0.00
P_2O_5	0.00	0.00	0.00	0.00	0.00	0.00	0.00	0.00	0.00	0.00	0.00	0.00	0.00	0.00	0.00
NiO	0.28	0.29	0.27	0.25	0.30	0.29	0.29	0.28	0.33	0.34	0.36	0.34	0.24	0.30	0.27
Cr_2O_3	0.16	0.29	0.21	0.38	0.30	0.19	0.20	0.25	0.06	0.26	0.27	0.20	0.22	0.17	0.20
[a]LOI	16.29	15.29	17.01	13.66	13.97	13.63	13.46	14.76	16.38	15.46	16.34	16.06	15.40	14.95	15.18
Total	99.70	99.76	99.69	99.60	100.09	99.47	99.54	99.69	99.60	98.94	99.66	99.40	99.82	99.75	99.79
Mg#	91.18	90.96	91.50	91.33	91.22	91.56	91.67	91.35	91.18	89.71	89.97	90.29	92.26	91.80	92.03
[b]%Serpentinization	80	70	93	75	80	80	65	77.57	93	85	90	89.33			0.00

Note: Data (in wt% oxides) from whole-rock analyses by XRF.
[a] Between 105° and 1030°C.
[b] Estimated from thin sections.

Table 5. Trace-element data for serpentinized ultramafic rocks and matrix samples from Hole 784A.

Core, section: Interval (cm):	36R-1, 107–109	37R-1, 6–9	38R-1, 66–68	38R-2, 92–95	42R-1, 5–8	45R-1, 98–100	45R-2, 44–44	Average harzburgite	40R-2, 41–43	41R-2, 98–100	42R-1, 39–41	Average dunite	38R-2, 29–31	40R-1, 84–87	Average matrix
Nb	tr	tr	tr	tr	tr	tr	tr	tr	tr	tr	tr	tr	tr	tr	tr
Zr	0	1	0	1	1	18	1	1	1	1	1	1	1	1	1
Y	nd	0	0	0	1	nd	0	0	nd	nd	0	0	1	0	1
Sr	2	3	3	4	5	5	5	4	3	3	3	3	4	4	4
Rb	0	0	0	0	0	nd	nd	0	0	0	nd	0	1	0	1
Zn	37	43	39	30	31	30	30	34	34	52	33	40	20	25	23
Cu	3	3	2	4	1	4	1	2	1	3	1	2	2	2	2
Ni	2214	2258	2139	1991	2327	2249	2259	2205	2534	2640	2819	2664	1897	2342	2120
Cr	1115	2012	1428	2585	2045	1310	1339	1691	444	1765	1871	1360	1539	1164	1352
V	19	45	23	29	36	32	36	31	7	4	19	10	20	12	16
TiO_2	0	0	0	0	0	0	0	0	0	0	0	0	0	0	0
Ce	nd	nd	nd	nd	nd	tr	tr	nd	tr	nd	tr	tr	tr	tr	tr
Ba	tr	11	12	tr	12	nd	nd	tr	nd	tr	11	tr	tr	tr	tr

Note: Data (in ppm) from whole-rock analyses by XRF; nd = not detected; tr = below detection limit (<2 ppm for Nb, <10 ppm for Ba and Ce).

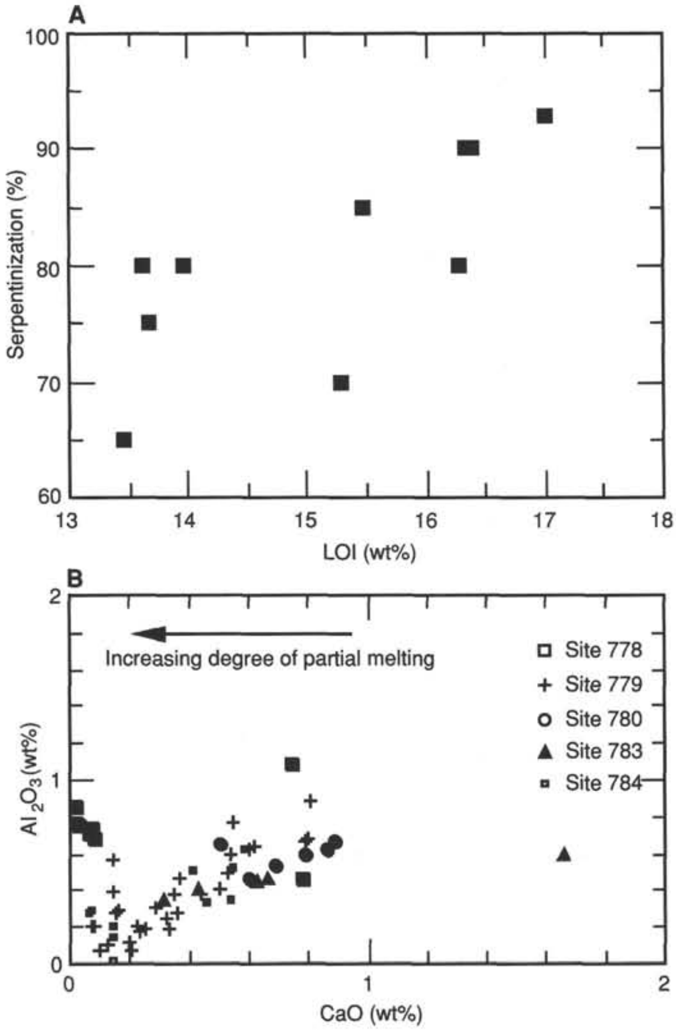

Figure 7. **A.** Modal percent of serpentinization vs. loss on ignition between 105° and 1030°C. **B.** Al_2O_3 vs. CaO for Sites 778 and 779 (Mariana seamount flank), 780 (Mariana seamount summit), and 783 and 784 (Izu-Bonin forearc).

ical errors. Strontium varies from 2 to 5 ppm, which is lower than the ultramafic concentrations at Sites 778 through 780 and Site 783. Average concentrations of vanadium in the harzburgites from Site 784 (31 ppm) are higher than the average concentrations in the dunites (10 ppm). There is no significant correlation between the geochemical parameters and depth.

Matrix Samples

Two samples (125-784A-38R-2, 29–31 cm, and 125-784A-40R-1, 84–87 cm) of the highly sheared serpentine matrix were analyzed by X-ray fluorescence (XRF). The bulk chemistry of these two samples is remarkably similar and deviates little from the average ultramafic values. The average weight percent values for SiO_2, Al_2O_3, Fe_2O_3, MgO, and CaO are 36.58, 0.26, 6.90, 40.21, and 0.13, respectively (Table 4). The values of chromium (1352 ppm) and nickel (2120 ppm) also fall within typical ranges for ultramafic rocks.

SEDIMENT/FLUID GEOCHEMISTRY

Sediment Geochemistry

Cores from Site 784 were analyzed on board the ship for inorganic carbon and for total carbon, nitrogen, and sulfur, using the techniques described in the "Explanatory Notes" (this volume). The organic carbon content was then calculated by difference. Results are presented in Table 6 and Figure 8.

The $CaCO_3$ content of the sediments, serpentine, and phacoidal sheared serpentine microbreccia is low, generally less than 0.3 wt%. Of 147 samples, only five have more than 1% $CaCO_3$; these are from about 1, 13, 269, and 321 mbsf. The sample from 321 mbsf has the highest $CaCO_3$ content, 11 wt%. It is from the uppermost part of the phacoidal sheared serpentine microbreccia of Unit II. In thickness and carbonate content, the $CaCO_3$-rich layer at 321 mbsf at Site 784 is similar to that encountered within a few meters of the seafloor in the serpentine sediments and flows at Sites 778, 779, and 780 on Conical Seamount in the Mariana forearc. Carbonate enrichment at the Conical Seamount sites takes the form of aragonite needles dispersed throughout the serpentine. These needles were tentatively interpreted as precipitates within a reaction front between bicarbonate-rich interstitial waters and calcium-rich ocean bottom water (see "Sediment/Fluid Geochemistry" section, "Site 780" chapter, this volume). The carbonate enrichment at the top of the serpentine unit at Site 784 takes the form of dispersed $CaCO_3$, rather than discrete aragonite needles. However, if needles were originally present, it is likely that they would have recrystallized. It is possible, therefore, that the serpentine at 321 mbsf at Site 784 became enriched in $CaCO_3$ when it was near the seafloor and that the interstitial waters at Site 784 once resembled those sampled from Conical Seamount during Leg 125, at least in having very high carbonate alkalinity. The waters at Site 784 are significantly different from those at Conical Seamount and do not have high alkalinity at the present, as will be shown in the "Fluid Geochemistry" section (this chapter).

The content of organic carbon in the cores at Site 784 nearly always exceeds that of inorganic carbon, varying between 0.2 and 0.7 wt%, except for a carbon-poor interval from 340 mbsf to the bottom of the hole. The nitrogen content varies from less than 0.01 to 0.3 wt% and generally correlates with that of organic carbon. Sulfur was detected in only five samples, from 234, 245, 254, 274, and 378 mbsf, where its concentration varies from 0.17 to 0.29 wt%.

Fluid Geochemistry

As at Sites 782 and 783, the concentration of methane measured on 5-cm^3 headspace samples is generally low, less than 20 μL/L. The sole exception is the deepest sample from Hole 784A, for which a concentration of 32 μL/L was obtained (Table 7). Methane was the only hydrocarbon detected.

Interstitial waters at Site 784 are similar to those at Site 783. The holes drilled at both sites penetrated glass-rich silty clays and claystones, underlain by phacoidal, sheared serpentine containing clasts mainly of harzburgite. The transition between these two units is more gradual at Site 784, where the units are separated by 18 m (303–321 mbsf) of interbedded claystone and silt-sized serpentine. As at Site 783, the composition of the interstitial waters at Site 784 changes abruptly between the claystone and the serpentine units, especially in terms of pH and silica. Values of pH increase to 9.6 in the serpentine and silica decreases to less than 10 μmol/kg (Table 8 and Fig. 9).

The changes in other dissolved species are less abrupt at Site 784 than at Site 783 only because the claystone is much thicker at Site 784, and many of the changes found at the boundary with the serpentine are extensions of changes that are already proceeding with depth in the claystone. This is the case for alkalinity, which has a concentration in waters within the serpentine of about one-half of that in seawater,

Table 6. Total nitrogen, sulfur, carbon, inorganic carbon, organic carbon, and carbonate carbon in cores at Site 784.

Core, section, interval (cm)	Depth (msbf)	Total nitrogen (wt%)	Total sulfur (wt%)	Total carbon (wt%)	Inorganic carbon (wt%)	Organic carbon (wt%)	$CaCO_3$ (wt%)
125-784A-							
1R-1, 74–76	0.74	0.15	nd	0.53	0.10	0.43	0.8
1R-CC, 22–24	1.16		0.23	1.9			
2R-1, 5–7	1.45	0.12	nd	0.36	0.04	0.32	0.3
3R-1, 74–76	11.64		0.04	0.3			
3R-2, 35–37	12.75	0.09	nd	1.37	1.14	0.23	9.5
3R-3, 67–69	14.57		0.11	0.9			
3R-4, 18–20	15.58		0.01	0.1			
4R-1, 31–33	20.71		0.09	0.7			
4R-2, 31–33	22.21	0.12	nd	0.35	0.01	0.34	0.1
4R-3, 31–33	23.71		0.08	0.7			
4R-4, 31–33	25.21		0.01	0.1			
6R-1, 76–78	40.26		0.01	0.1			
6R-2, 80–82	41.80	0.17	nd	0.56	0.04	0.52	0.3
6R-3, 85–87	43.35		0.03	0.2			
6R-4, 90–92	44.90		0.02	0.2			
6R-5, 91–93	46.41		0.01	0.1			
6R-6, 45–47	47.45		0.06	0.5			
7R-1, 67–69	49.77		0.06	0.5			
7R-2, 65–67	51.25	0.11	nd	0.31	0.02	0.29	0.2
7R-3, 65–67	52.75		0.05	0.4			
8R-1, 69–71	59.49		0.02	0.2			
8R-2, 106–108	61.36	0.18	nd	0.82	0.10	0.72	0.8
8R-3, 52–54	62.32		0.02	0.2			
8R-4, 56–58	63.86		0.02	0.2			
8R-5, 51–53	65.31		0.01	0.1			
9R-1, 85–87	69.35		0.01	0.1			
9R-2, 85–87	70.85	0.12	nd	0.36	0.01	0.35	0.1
9R-3, 77–79	72.27		0.01	0.1			
9R-4, 42–44	73.42		0.01	0.1			
9R-5, 27–29	74.77		0.01	0.1			
10R-1, 49–51	78.59		0.01	0.1			
10R-2, 59–61	80.19	0.14	nd	0.38	0.01	0.37	0.1
10R-3, 103–105	82.13		0.01	0.1			
10R-4, 80–82	83.40		0.01	0.1			
12R-1, 58–60	97.98		0.01	0.1			
12R-2, 44–46	99.34	0.12	nd	0.35	0.01	0.34	0.1
13R-1, 36–38	107.46	0.12	nd	0.38	0.01	0.37	0.1
14R-1, 97–99	117.67		0.09	0.8			
14R-2, 63–65	118.83	nd	nd	0.46	0.01	0.45	0.1
14R-3, 30–32	120.00		0.01	0.1			
14R-4, 30–32	121.50		0.01	0.1			
14R-5, 70–72	123.40		0.01	0.1			
15R-1, 78–80	127.18		0.01	0.1			
15R-2, 56–58	128.46	0.13	nd	0.34	0.01	0.33	0.1
15R-2, 94–96	128.84		0.01	0.1			
15R-4, 96–98	131.86		0.01	0.1			
15R-5, 79–81	133.19		0.03	0.2			
15R-6, 79–81	134.69		0.01	0.1			
15R-7, 39–41	135.79		0.01	0.1			
16R-1, 56–68	136.56		0.01	0.1			
16R-2, 56–58	138.06	0.12	nd	0.31	0.01	0.30	0.1
16R-3, 56–58	139.56		0.01	0.1			
16R-4, 56–58	141.06		0.01	0.1			
16R-5, 56–58	142.56		0.01	0.1			
16R-6, 41–43	143.91		0.01	0.1			
16R-7, 41–43	145.41		0.02	0.2			
17R-1, 86–88	146.46		0.01	0.1			
17R-2, 48–50	147.58	0.11	nd	0.23	0.02	0.21	0.2
17R-3, 51–53	149.11		0.02	0.2			
17R-4, 51–53	150.61		0.02	0.2			
17R-5, 34–36	151.94		0.02	0.2			
18R-1, 90–92	156.20		0.01	0.1			
18R-2, 121–123	158.01	0.12	nd	0.25	0.02	0.23	0.2
18R-3, 105–107	159.35		0.01	0.1			
18R-4, 82–84	160.62		0.01	0.1			
18R-5, 118–120	162.48		0.02	0.2			
18R-6, 86–88	163.66		0.01	0.1			
18R-7, 18–20	164.48		0.01	0.1			
19R-1, 56–58	165.56		0.02	0.2			
19R-2, 36–38	166.86	nd	nd	0.40	0.01	0.39	0.1
20R-1, 104–106	175.74		0.01	0.1			
20R-2, 120–121	177.40	nd	nd	0.32	0.01	0.31	0.1
20R-3, 109–111	178.79		0.01	0.1			
20R-4, 48–49	179.68		0.01	0.1			

Table 6 (continued).

Core, section, interval (cm)	Depth (msbf)	Total nitrogen (wt%)	Total sulfur (wt%)	Total carbon (wt%)	Inorganic carbon (wt%)	Organic carbon (wt%)	$CaCO_3$ (wt%)
20R-5, 56–58	181.26		0.07	0.6			
21R-1, 108–110	185.48		0.01	0.1			
21R-2, 65–67	186.55	nd	nd	0.27	0.01	0.26	0.1
21R-3, 21–23	187.61		0.01	0.1			
21R-4, 106–108	189.96		0.01	0.1			
21R-5, 18–20	190.58		0.01	0.1			
22R-1, 96–98	194.96		0.01	0.1			
22R-2, 96–98	196.46	nd	nd	0.43	0.06	0.37	0.5
22R-3, 124–126	198.24		0.03	0.2			
22R-4, 114–116	199.64		0.01	0.1			
22R-5, 67–69	200.67		0.01	0.1			
22R-6, 66–68	202.16		0.01	0.1			
23R-1, 133–135	204.93		0.01	0.1			
23R-2, 104–106	206.14	0.30	nd	0.69	0.02	0.67	0.2
23R-3, 30–33	206.90		0.01	0.1			
24R-1, 34–36	213.54		0.02	0.2			
24R-2, 41–43	215.11	0.24	nd	0.57	0.02	0.55	0.2
24R-3, 110–112	217.30		0.02	0.2			
24R-4, 127–129	218.97		0.02	0.2			
24R-5, 29–31	219.49		0.02	0.2			
24R-6, 18–20	220.88		0.02	0.2			
25R-1, 59–61	223.49		0.02	0.2			
26R-1, 95–97	233.45		0.02	0.2			
26R-2, 40–42	234.40	0.21	0.29	0.49	0.01	0.48	0.1
27R-1, 117–119	243.27		0.01	0.1			
27R-2, 104–106	244.64	0.16	0.24	0.42	0.02	0.40	0.2
27R-3, 82–84	245.92		0.01	0.1			
27R-4, 53–55	247.13		0.02	0.2			
27R-5, 80–82	248.90		0.03	0.2			
28R-1, 110–112	252.90		0.02	0.2			
28R-2, 86–88	254.16	0.21	0.29	0.50	0.01	0.49	0.1
28R-3, 21–23	255.01		0.09	0.7			
29R-1, 99–101	262.39		0.01	0.1			
29R-2, 107–109	263.97	0.12	nd	0.41	0.02	0.39	0.2
29R-3, 57–59	264.97		0.03	0.2			
29R-4, 49–51	266.39		0.02	0.2			
29R-5, 55–57	267.95		0.04	0.3			
29R-6, 28–30	269.18		0.22	1.8			
29R-7, 39–41	270.79		0.09	0.7			
30R-1, 34–36	271.44		0.01	0.1			
30R-2, 93–95	273.53	0.19	0.27	0.47	0.07	0.40	0.6
30R-3, 82–84	274.92		0.02	0.2			
30R-4, 69–72	276.29		0.02	0.2			
30R-5, 48–50	277.58		0.02	0.2			
31R-1, 31–34	281.11		0.02	0.2			
31R-2, 83–86	283.13	0.26	nd	0.57	0.03	0.54	0.3
31R-3, 81–83	284.61		0.02	0.2			
32R-1, 86–88	291.26		0.02	0.2			
32R-2, 99–101	292.89	0.19	nd	0.44	0.02	0.42	0.2
32R-3, 70–72	294.10		0.03	0.2			
32R-4, 43–45	295.33		0.03	0.2			
32R-5, 24–26	296.64		0.03	0.2			
32R-6, 112–114	299.02		0.03	0.2			
32R-7, 33–35	299.73		0.03	0.2			
33R-1, 33–34	300.33		0.03	0.2			
33R-2, 122–123	302.72	0.15	nd	0.31	0.01	0.30	0.1
33R-3, 35–36	303.35		0.01	0.1			
33R-4, 50–52	305.00		0.01	0.1			
34R-1, 11–13	309.81		0.02	0.2			
34R-2, 31–33	311.51	0.20	nd	0.43	0.01	0.42	0.1
35R-1, 131–133	320.61		0.22	1.8			
35R-2, 22–24	321.02	nd	nd	1.76	1.32	0.44	11.0
36R-1, 33–35	329.33		0.05	0.4			
37R-1, 71–73	339.41		0.05	0.4			
37R-2, 26–28	340.46	nd	nd	0.26	0.05	0.21	0.4
39R-1, 80–82	358.70		0.04	0.3			
39R-2, 83–85	360.23	nd	nd	0.19	0.04	0.15	0.3
40R-1, 94–97	368.44		0.04	0.3			
41R-1, 70–72	378.00	nd	0.17	0.25	0.04	0.21	0.3
42R-1, 80–82	387.70		0.06	0.5			
42R-2, 41–43	388.81	nd	nd	0.20	0.06	0.14	0.5
43R-1, 103–105	397.63		0.07	0.6			
43R-2, 98–100	399.08	0.06	nd	0.18	0.08	0.10	0.7
43R-3, 60–62	400.20		0.08	0.7			

Note: nd = not detected.

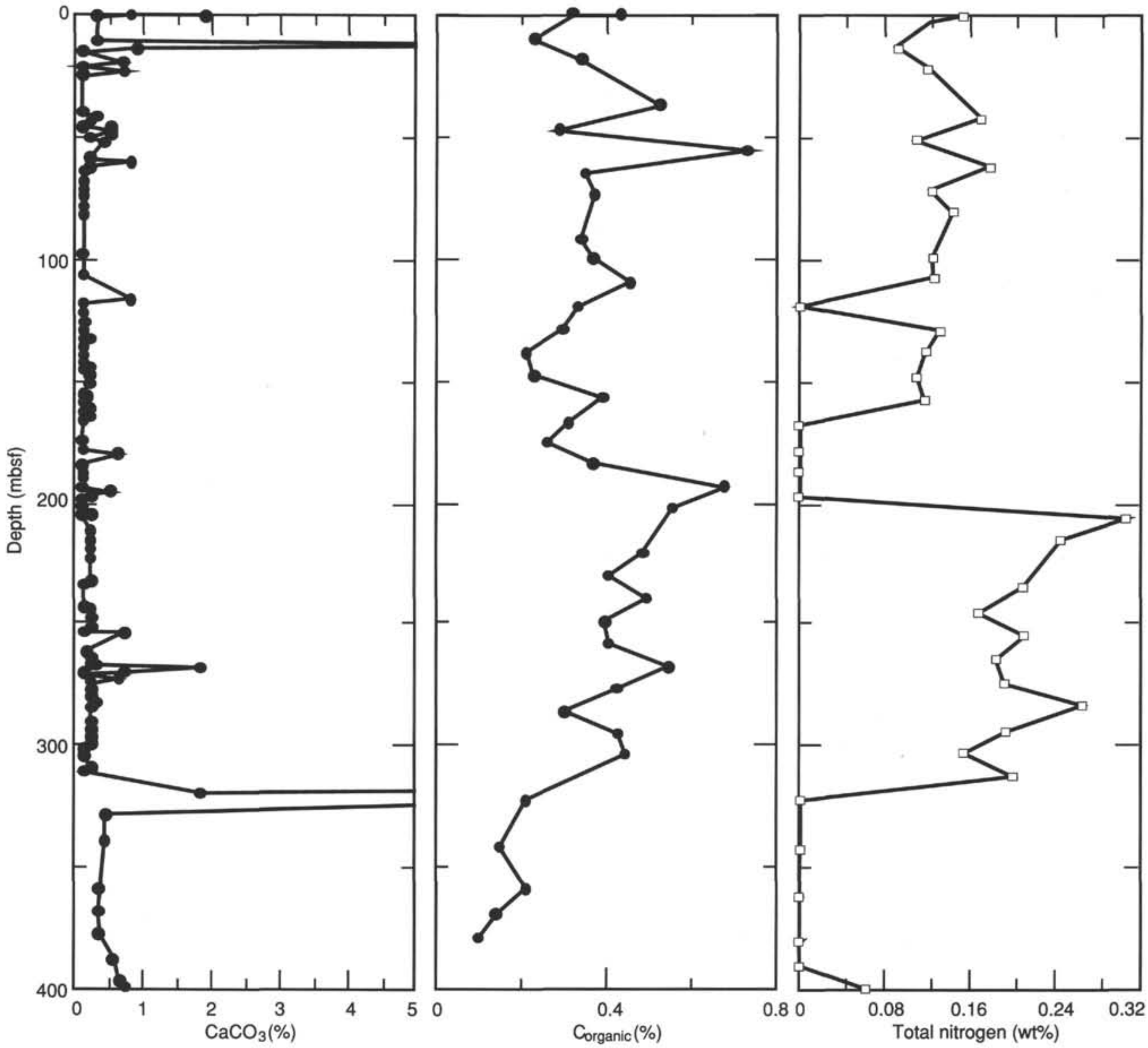

Figure 8. Weight percent of calcium carbonate, total organic carbon, and total nitrogen in sediments at Site 784.

and sulfate, which decreases to 7 mmol/kg with a distinct break in slope at the serpentine boundary (Fig. 9). Also continuing the trend established in the claystone but showing a break in slope at the boundary are calcium, which increases to 57 mmol/kg within the serpentine; magnesium, which decreases to less than 1 mmol/kg; and sodium, which decreases to 452 mmol/kg (Fig. 9). The change in sodium within the serpentine at Site 784 is the opposite of that seen at Site 783, where sodium increases. Ammonia and potassium stabilize at a nearly constant values within the serpentine, after decreasing with depth throughout the lower part of the claystone.

Chlorinity shows no obvious change with depth at Site 784, except for a possible increase within the upper 45 mbsf (Fig. 9). Bromide may increase below 234 mbsf, but the data are so scattered that we cannot be certain of this. As at Site 783, the decrease in salinity with depth results mainly from the decrease in sulfate.

The major difference between the interstitial waters at Site 784 and those at Sites 782 and 783 is the greater effect of bacterial sulfate reduction within the thicker claystone at Site 784. This reduction causes sulfate to decrease markedly with depth within the claystone as well as within the serpentine (Fig. 9). The same bacterial reactions that reduce sulfate and oxidize organic matter cause the largest maxima in alkalinity and ammonia to develop within the upper sediments at Site 784. The waters within the thicker claystone unit at Site 784 also display higher gradients in calcium and magnesium and a greater decrease in potassium than those at Site 783.

As at Site 783, the changes in pore-water composition between the claystone and the serpentine almost certainly result from ongoing reactions between seawater-derived solutions and the partially serpentinized peridotite. The pore waters from Site 784 support the conclusion reached previously ("Sediment/Fluid Geochemistry" section, "Site 783" chapter, this volume) that these reactions consume H^+, silica, sulfate, and magnesium, produce calcium, and conserve chlorinity. The effect of serpentinization reactions on alkalinity, ammonia, and potassium is less evident at Site 784 than at Site 783 because these species already show large changes within

Table 7. Results of headspace-gas analyses of cores at Site 784.

Core, section, interval (cm)	Depth (mbsf)	Methane (μL/L)[a]	(μM)[b]
125-784A-			
2R-1, 19–20	1.60	10	0.9
3R-3, 0–3	13.92	11	0.9
4R-3, 0–3	23.42	11	1.0
6R-5, 0–3	45.52	13	1.2
7R-2, 0–3	50.62	15	1.4
8R-5, 0–3	64.82	15	1.3
9R-2, 0–3	70.02	15	1.3
10R-2, 0–3	79.62	13	1.2
12R-2, 0–3	98.92	14	1.3
14R-3, 0–3	119.72	11	1.0
16R-6, 0–3	143.52	11	0.9
19R-2, 148–150	167.99	12	1.1
20R-4, 0–3	179.21	15	1.3
21R-2, 0–3	185.92	12	1.0
22R-4, 0–3	198.52	11	1.0
23R-2, 0–3	205.11	11	1.0
26R-2, 0–3	234.02	10	0.9
29R-5, 0–3	267.41	10	0.9
32R-6, 0–3	297.91	8	0.7
36R-1, 0–3	329.02	16	1.4
37R-2, 0–3	340.22	13	1.2
39R-2, 112–114	360.53	13	1.2
42R-2, 0–1	388.41	15	1.3
43R-3, 0–1	399.61	32	2.9

[a] Microliters of methane per liter of wet sediment or wet unconsolidated serpentine, assuming a sample volume of 4.2 cm^3 of sediment or serpentine.

[b] Micromoles of methane per liter of interstitial water, assuming a porosity of 50%.

the overlying claystone at Site 784. The effect on sodium is unclear because sodium increases within the serpentine at Site 783, but decreases at Site 784. As at Site 783, the pore waters at Site 784 contain no obvious component of low-chlorinity, hydrocarbon-rich water from a deep source, such as was proposed to explain the composition of pore waters at Conical Seamount in the Mariana forearc (see "Sediment/Fluid Geochemistry" section, "Site 780" chapter, this volume).

STRUCTURAL STUDIES

At Site 784, we observed a wide variety of deformational features within the unlithified and partially lithified sediments of Unit I. Many of these features are closely associated with water-escape structures. Within the underlying serpentine microbreccia of Unit II, we observed pure- and simple-shear and convolute structures. The textures and rheological properties of the serpentine and microbreccia, as well as the structures developed within them, are very similar to those at Site 779 on the flank of Conical Seamount.

Deformation in Unlithified Sediments

Deformation features are rare in the unconsolidated silty clay of Subunit IA. However, between 54 and 60 cm in Section 125-784A-6R-5, we observed a set of *en echelon,* subvertical, sigmoidal veinlets (Fig. 10). This veinlet set exhibits a geometry very similar to that of the *en echelon,* vein-filled, "tension-gash" sets common in well-lithified rocks, especially those in the lower greenschist facies. The veinlets are 3 to 4 cm long and about 1 mm wide. Observation under the binocular microscope shows that the veinlets are zones of greatly increased porosity. We interpret this vein set as having developed when the unlithified sediment was subjected to subhorizontal simple shear and formed sigmoidal zones of extensional or reduced compressional stress into which pore water flowed. This influx of fluid caused the consolidating sediment to disaggregate, increasing its porosity. Similar structures were observed in unlithified sediment on the inner slope of the Middle America Trench during Deep Sea Drilling Project (DSDP) Leg 67 (Cowan, 1982).

Deformation in Partially Lithified Sediments

Deformation of the more consolidated vitric siltstones of Subunit IB includes the following (Fig. 11): (1) subhorizontal to subvertical water-escape structures, along some of which primary sedimentary structures such as ash layers or centimeter-sized burrows have been offset; (2) *en echelon* tension veinlets, some of which have acted as microfaults and are associated with microlithon rotation; (3) *en echelon* sets of microfaults a few centimeters long with offsets of a few millimeters; (4) parallel, gently dipping veinlets, spaced 2 to 5 mm apart and forming sets distributed throughout the entire core over intervals of a few decimeters; (5) small, isolated normal and reverse faults; and (6) ductile shear bands.

Water-escape structures are abundant and generally consist of centimeter- to decimeter-wide pipes or dikes filled with homogeneous light-colored claystone that is distinct from the surrounding darker, burrowed claystones. Sedimentary layering is offset along many of these structures. In a spectacular example within Section 125-784A-28R-2, 42–62 cm (Fig. 12), a subhorizontal ash layer and a burrow were offset about 2 cm along a 5- to 10-mm-wide, subvertical, dikelike water-escape structure. This water-escape structure contains laminae defined by variations in clast content within the filling of the pipe; we interpret these laminae as flow-differentiation bands that formed when fluid escaped. In other instances, water-escape structures terminate along faults. Between 55 and 80 cm in Section 125-784A-32R-2, a 20-cm-long pipe endsabruptly along a low-angle fault. The fault plane may have served as a conduit for water.

Sets of sigmoidal, *en echelon,* tension veinlets, similar to those described previously, are common in the interval between Core 125-784A-22R and Core 125-784A-32R (Fig. 13). Most of the veinlet sets are not associated with faults and thus represent brittle-ductile shear bands. The size of the veinlets (7 to 10 cm long, about 1 mm wide) and their spacing (5 to 10 mm) are remarkably constant within this interval. The veins exhibit generally a simple shape, with a regular curvature and sharp tails. Locally, veins with forked tails were observed. In some sets of tension veinlets, the central part of the set is connected by a second (subsequent?) set of smaller veinlets that have a slightly different orientation. This probably indicates multistage creep along the shear zone. Although the curvature of the sigmoidal veinlets indicates that reverse movements have also taken place, normal movement is much more common, indicating lateral extension with respect to the core axis.

In some cases (e.g., Section 125-784A-22R-4, 130–140 cm), sigmoidal veinlets have served as microfaults. These exhibit the same attitude, size, and shape as the tension veinlets described previously. We postulate that these microfaults are a smaller-scale version of the water-escape dike with offsets described in the preceding text.

In Section 125-784A-27R-5, between 10 and 20 cm, steeply dipping (65° to 70°) sediments are cut by *en echelon* normal microfaults having offsets of a few centimeters. These microfaults are not sigmoidal, and we regard them as a somewhat different phenomenon from those already described.

Numerous parallel, gently dipping veinlets occur in the basal part of Subunit IB, especially in Section 125-784A-32R-4. The veinlets crosscut the core from one edge to the other and are regularly spaced from a few millimeters to 1 cm

Table 8. Composition of interstitial waters from cores at Site 784.

Sample number	Core, section, interval (cm)	Depth (mbsf)	Volume (mL)	Squeeze temperature (°C)	pH	Salinity (R.I., %)	Salinity (calcium, %)	Chlorinity (mmol/kg)	Alkalinity (meq/kg)	Sulfate (mmol/kg)	Sodium (mmol/kg)	Potassium (mmol/kg)
Surface seawater (17 March 1989)					8.25	35.6	34.65	539.2	2.689	27.28	462.0	10.11
IW-1	3R-2, 140–150	13.85	58	3	7.95	35.8	35.06	546.5	4.257	26.14	469.5	10.22
IW-2	4R-2, 140–150	23.35	58	3	7.84	36.5	35.05	548.4	3.923	25.42	470.1	10.05
IW-3	6R-4, 140–150	45.45	60	3	8.19	36.3	35.32	552.3	4.417	25.07	476.1	9.87
IW-4	8R-4, 140–150	64.75	55	4	8.21	35.0	34.75	549.4	4.260	22.05	470.1	9.52
IW-5	10R-1, 140–150	79.55	45	5	8.17	35.5	34.99	550.4	4.290	23.34	474.6	8.81
IW-6	14R-1, 140–150	118.15	51	5	8.07	35.2	34.73	550.4	4.273	21.08	472.5	8.06
IW-7	16R-5, 140–150	143.45	55	8	8.00	35.5	34.74	549.4	3.447	21.82	472.1	8.01
IW-8	19R-3, 0–10	168.05	48	8	8.17	35.0	34.28	543.6	3.438	20.58	467.0	7.71
IW-9	22R-3, 140–150	198.45	54	8	8.00	34.0	34.55	550.4	3.249	19.61	470.9	6.90
IW-10	26R-1, 140–150	233.95	33	9	7.65	34.3	34.46	550.4	2.227	19.23	471.1	7.14
IW-11	29R-4, 140–150	267.35	35	10	8.07	34.8	34.20	549.4	1.911	17.84	466.3	6.66
IW-12	32R-5, 140–150	297.85	38	10	7.82	34.5	34.03	550.4	1.225	16.38	465.9	5.95
IW-13	34R-3, 0–15	312.78	15	9	7.53	33.8	33.07	540.7	0.517	14.36	450.6	4.61
IW-14	35R-1, 135–150	320.73	30	10	8.16	34.2	33.63	548.4	0.588	14.76	462.2	5.93
IW-15	39R-2, 0–15	359.48	16	11	9.14	35.4	33.37	546.5	1.404	11.48	460.7	5.96
IW-16	40R-1, 135–150	368.93	15	10	9.25	35.5	33.56	553.3	1.362	9.78	455.3	5.31
IW-17	41R-1, 92–107	378.30	22	10	9.61	34.3	33.49	550.4	1.314	10.44	455.0	5.52
IW-18	42R-1, 135–150	388.33	16	10	9.59	34.3	32.94	549.4	0.650	7.00	453.0	5.16
IW-19	43R-2, 135–150	399.53	18	10	9.52	35.0	33.48	552.3	1.625	9.33	452.1	5.48

apart. Otherwise, undeformed burrows exhibit both normal and reverse offsets along the veins within a single set. Because the true orientation of the vein sets is unknown, it is impossible to determine whether these structures represent larger-scale structures similar to the *en echelon* veinlet sets previously described (although with overall subvertical, rather than subhorizontal, movement) or whether they are simply a series of discrete microfaults.

Isolated faults are common throughout Subunit IB. Spectacular examples have been encountered in Sections 125-784A-20R-3, 55–80 cm, (Fig. 14) and 125-784A-32R-2, 80–105 cm. Because the offsets along the fault planes are greater than

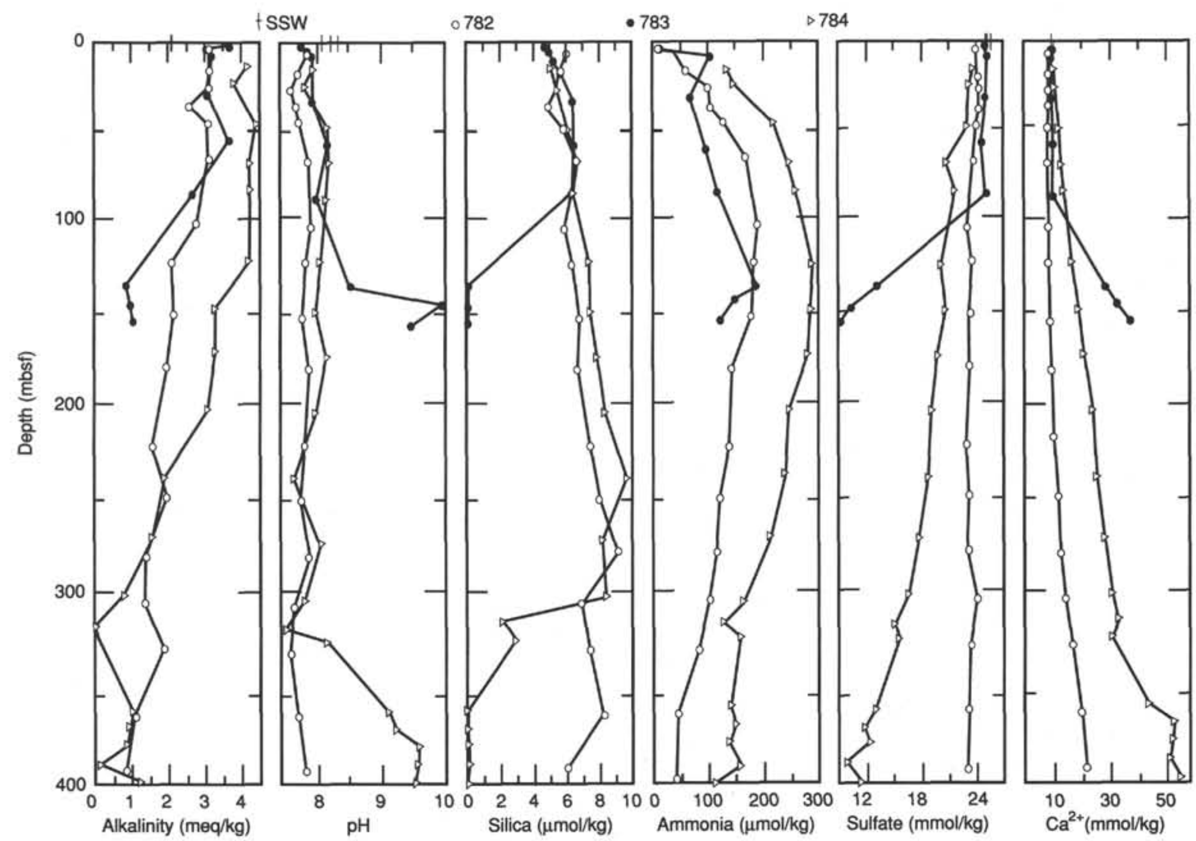

Figure 9. Composition of interstitial waters from sediments at Site 784 compared with that from Sites 782 and 783 and with surface seawater collected 22 February and 4 and 17 March 1989 (crosses).

Table 8 (continued).

Calcium (mmol/kg)	Magnesium (mmol/kg)	Bromide (mmol/kg)	Silica (μmol/kg)	Ammonia (μmol/kg)	Hydrogen Sulfide (μmol/kg)
10.18	52.48	0.81	0	10	
11.72	49.93	0.84	523	134	
12.10	49.40	0.77	557	150	
13.50	46.98	0.85	621	221	
14.29	44.78	0.84	680	246	
15.19	43.80	0.78	658	261	
18.10	40.03	0.80	749	290	
20.23	37.98	0.76	749	288	<3
22.15	34.57	0.81	792	282	
25.22	32.28	0.78	843	250	
26.65	29.74	0.83	972	241	
29.52	27.51	0.93	831	216	
31.79	24.46	0.83	854	172	
34.35	22.99	0.87	224	130	
32.02	23.20	0.89	304	160	
45.19	6.90	0.96	12	142	
54.43	2.36	0.91	6	150	
53.69	2.32	0.86	12	136	
52.87	0.08	0.92	18	161	
56.73	0.77	0.88	2	114	

the cored fault lengths, the true displacement cannot be determined. No offset sedimentary markers were observed; therefore, the sense of movement along the faults also remains unknown.

Sedimentary lamination at Site 784 is subhorizontal in the upper 190 mbsf of the sediments and from about 310 to 320 mbsf in the serpentine. However, from 190 to 275 mbsf

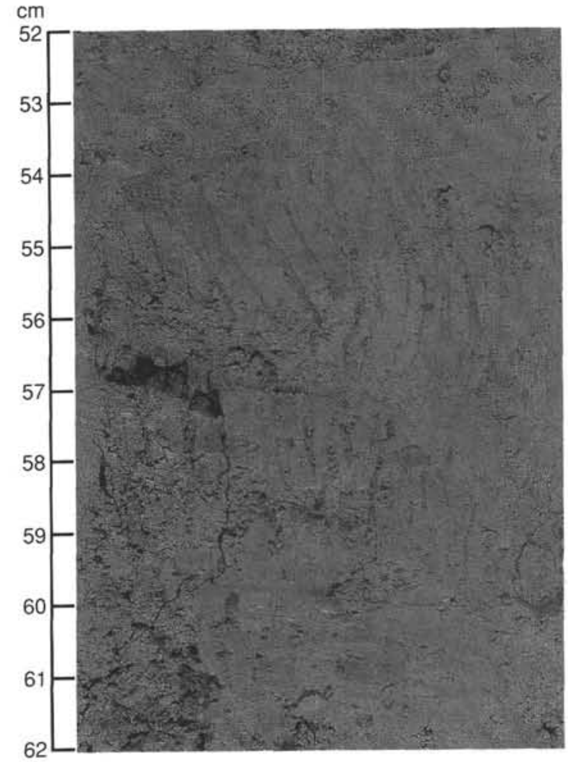

Figure 10. Set of *en echelon* sigmoidal veinlets in unconsolidated sediments (Section 125-784A-6R-5, 52–62 cm).

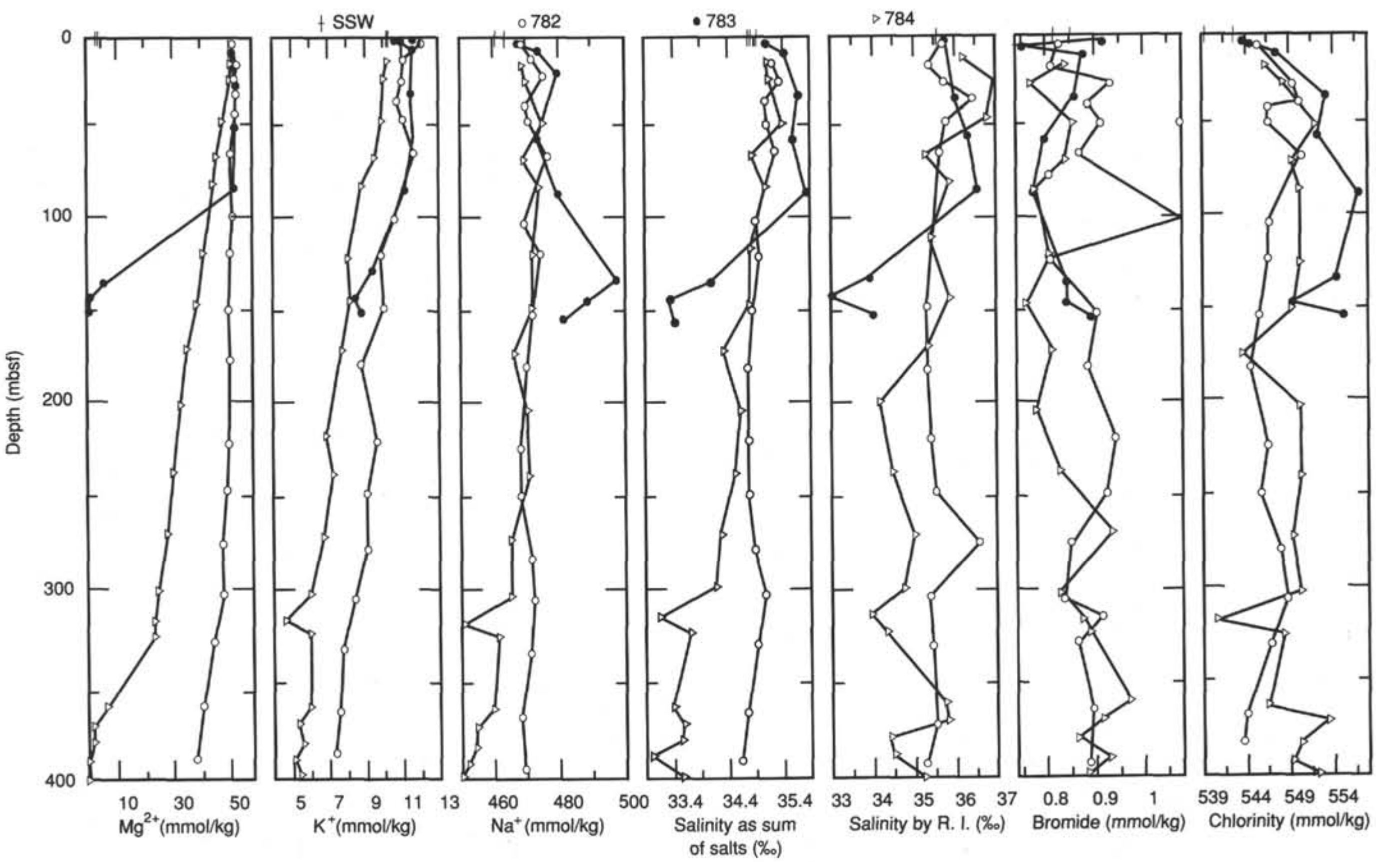

Figure 9 (continued).

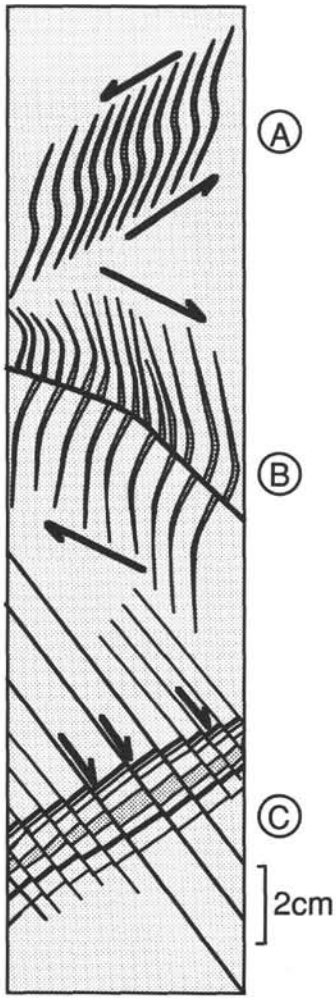

Figure 11. Schematic representation of the main post-depositional tectonic structures in the unconsolidated and partially lithified sediments of Unit I at Site 784. **A.** *En echelon* sigmoidal tension veinlets (no associated discrete fault plane). **B.** *En echelon* tension veinlets crosscut by an associated fault. **C.** Set of microfaults (note lack of microlithon rotation). **D.** *En echelon* tension veinlets with rotated microlithons. **E.** Set of parallel veinlets crosscutting the core.

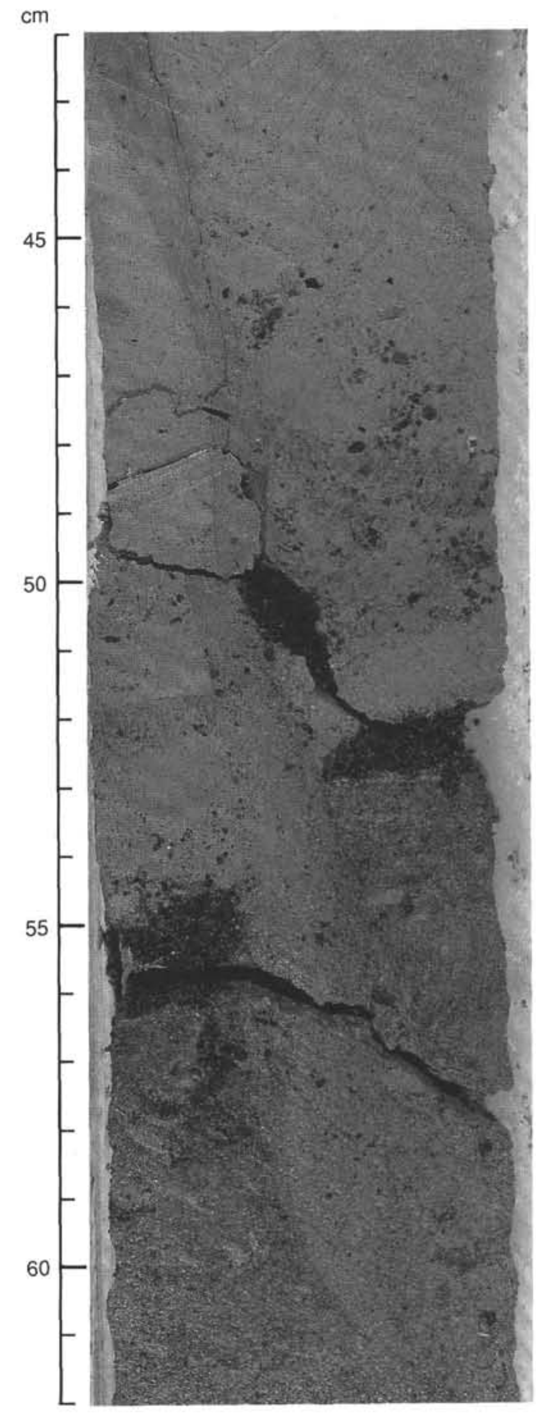

Figure 12. Water-escape dike or pipe offsetting burrows and an ash layer (Section 125-784A-28R-2, 42–62 cm).

(Sections 125-784A-21R-4 to 125-784A-30R-4), and possibly as deep as 295 mbsf (Section 125-784A-32R-2), sedimentary laminations dip consistently about 35°. We were unsuccessful in locating exactly the discrete faults that bound this moderately dipping interval. It probably represents a tilted fault block or slump block that was buried by later sedimentation.

A subhorizontal ductile shear zone is present at 112 to 115 cm in Section 125-784A-24R-4 (Fig. 15). In many ways, this shear zone is similar to those observed in crystalline rocks that have undergone high-temperature deformation. The zone contains laminae and burrows that have been transformed into characteristic sigmoidal shapes by ductile deformation. Deformation is confined to a sharply delimited band 3 cm thick. Unlike most high-grade ductile shear zones, however, deformation appears to decrease in the center of the zone and to increase outward toward the boundary surfaces, which are zones of narrowly concentrated shear and may be defined as faults. Sigmoidal laminae bend into these surfaces and are sheared out along them.

Where possible, we performed detailed three-dimensional measurements of the main faults and axial planes of the sets of tension veinlets. The results are plotted on a stereonet (Fig. 16). In this lower-hemisphere stereonet, the vertical axis (plunging at 90° into the net) corresponds to the true vertical (i.e., the long axis of the cores). The north and south directions on the net correspond to the left and right sides of the sawn face of the archive half of the core, and the east and west directions correspond to vectors plunging vertically into the sawn faces of the archive and working halves, respectively.

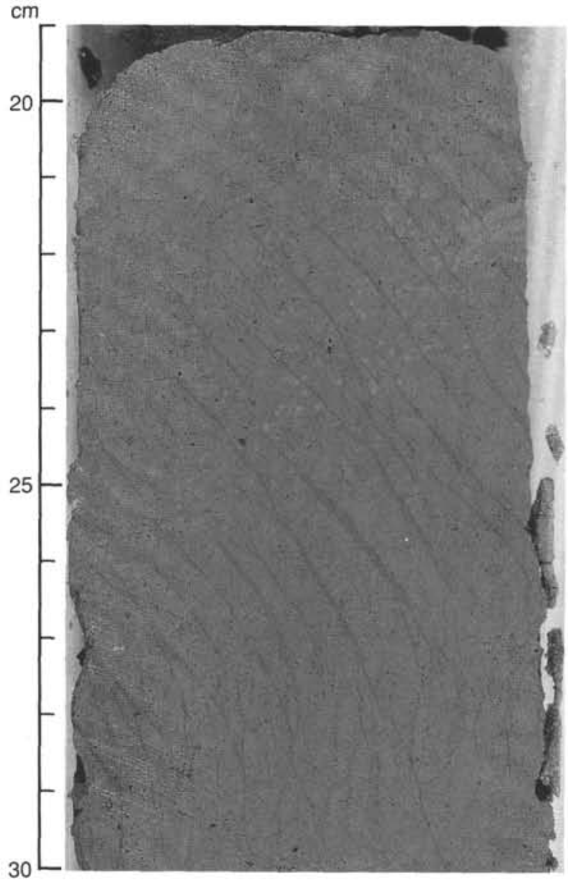

Figure 13. Set of *en echelon* sigmoidal tension veinlets (Section 125-784A-22R-3, 19–30 cm).

Thus, dips plotted on the stereonet represent true dips with respect to horizontal. Almost all faults dip between 30° and 60°, and the majority are in the lower part of this range. Dispersion of the measurements with respect to the vertical axis of the diagram may reflect the rotation of the cores during drilling, but also may indicate variability in the strikes of the fault planes. However, the uniformity of strike in many individual core sections suggests that most faults have about the same orientation.

In conclusion, most of the structures observed in the sediments of Unit I represent extensional processes. The close association of water-escape structures and brittle deformation shows that dewatering, lithification, and tectonism acted contemporaneously. Similar structures were observed at convergent margins on DSDP Legs 56 and 57 near the Japan Trench (Arthur et al., 1980), Leg 67 near the Middle America Trench (Cowan, 1982; Dengo, 1982), and Leg 78A on Barbados Ridge (Cowan et al., 1984).

Deformation in Serpentine Sediments and Microbreccias

Subunit IC and Unit II at Site 784 contain many types of variably sheared clastic serpentine sediments that were recovered at the previous Sites 778, 779, 780, and 783. The serpentine microbreccias exhibit convolute bedding and plastic folding. Phacoidal, sheared serpentine is abundant; most of the phacoids are soft, sheared clasts. Some have asymmetrical shapes, indicating deformation by simple shear. Variously sized blocks of hard, dark green serpentinized harzburgite contain abundant anastomosing asbestos veins and veinlets.

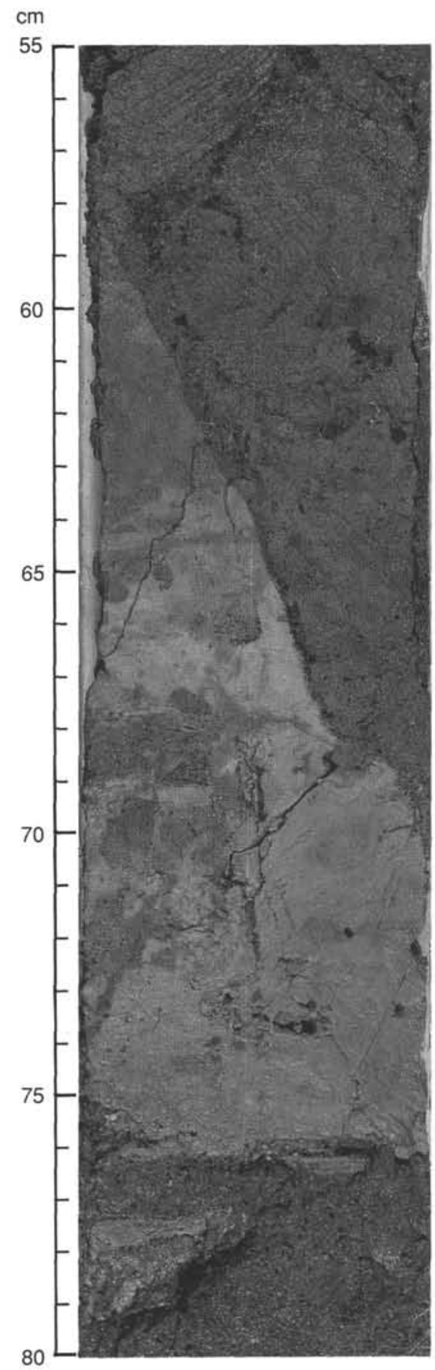

Figure 14. Fault with unknown displacement (Section 125-784A-20R-3, 55–80 cm).

In Subunit IC, the interlayering of poorly sorted, clastic, serpentine sediments bearing coarse, angular fragments with much better sorted, finer-grained, volcanogenic/pelagic sediments (see "Lithostratigraphy" section, this chapter) provides good evidence for interfingering between locally derived serpentinite debris flows and sediment distally derived from arc-related volcanoes. Moreover, these interlayered clastic serpentines, which are as thin as 30 cm, contain weakly to well-developed phacoidal textures, showing that this fabric can be preserved during downslope flow and may even have formed at that time. The individual units of different serpentine types (for instance, convolute zones, relatively unsheared

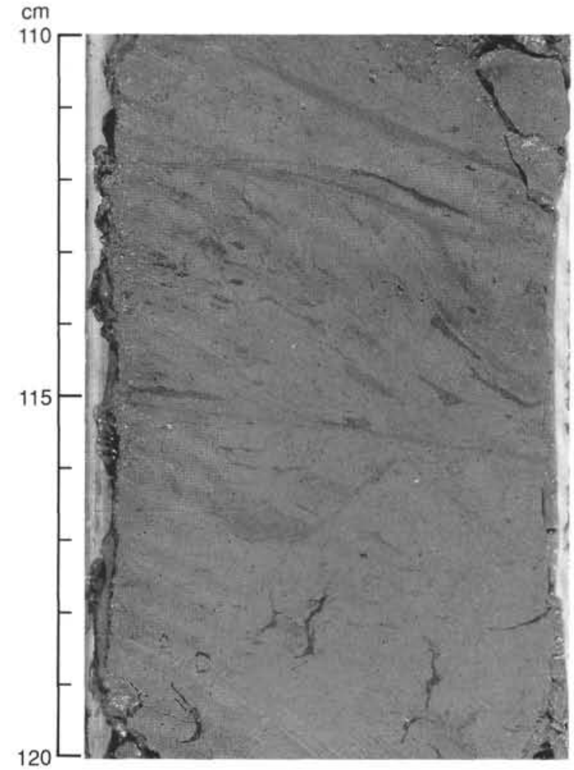

Figure 15. Subhorizontal ductile shear zone (Section 125-784A-24R-4, 110–120 cm).

sediment layers, and block-rich layers) are thinner at Site 784 than at the other sites, possibly because Site 784 (at the foot of the seamount) is relatively far from the probable sources of the serpentinite materials.

Within the cores, we observed intervals of clast-supported, matrix-poor breccias a few tens of centimeters thick. These clast-rich breccias are distinct from the convolute, matrix-rich microbreccias; we think that they may represent talus deposits. *In-situ* serpentinization, hydration, and fragmentation of matrix and clasts are continuing in the serpentinites we studied. As large blocks continue to serpentinize and fragment, they may provide a source for the breccias we describe here.

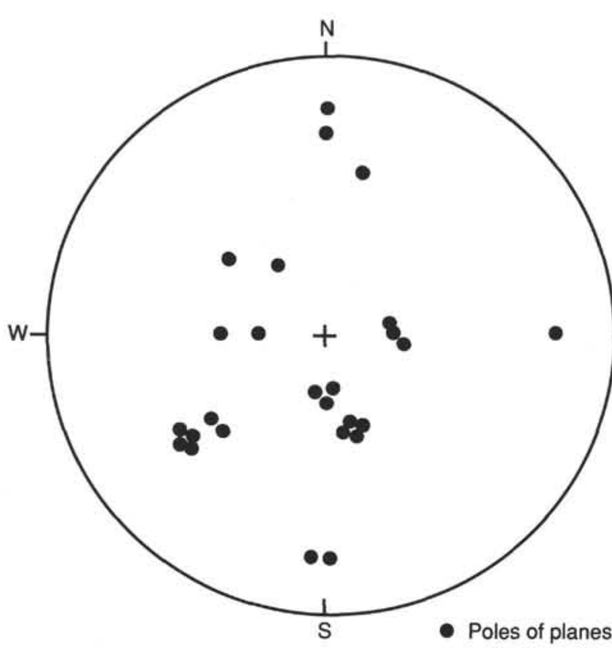

Figure 16. Orientation of main faults in Unit I plotted on a lower hemisphere stereonet. Vertical axis of stereonet = vertical axis of core; points = poles of planes.

Deformation in Serpentinization Fabrics

The general fabric and the microfabric of these rocks are similar to the fabric of the serpentinites at previous sites. Fiber haloes observed in thin sections of Site 784 serpentinites are highly variable and may be either isotropic or anisotropic. Many of them are quite deformed. This suggests that serpentinization occurred under both isotropic and anisotropic stress fields. The orientations of veins and fractures in the biggest blocks drilled at the bottom of the hole in Sections 125-784-45R-1 and 125-784-45R-2 vary from subhorizontal to subvertical. As with the microscopic fiber haloes, development of fiber veins of serpentine is probably associated with volume increase during serpentinization. The presence of veins with a wide range of orientations suggests that expansion was approximately isotropic and, hence, that at least this stage of serpentinization took place under low deviatoric stresses.

Deformation Fabrics in Pre-Serpentinization Peridotites

As with Site 783, the advanced state of serpentinization recorded at Site 784 prevented any systematic observation of high-temperature deformation textures. The few features remaining, like those at Site 783, are compatible with the tectonized nature of the primary peridotites.

Rheology of Sediments and Serpentine Material

Stress-strain tests were performed on the unlithified materials recovered at Site 784 using a Wykeham-Farrance torsion-vane test apparatus. Stress measurements for the samples tested are shown in Table 9, and a typical stress-strain curve is plotted in Figure 17, from which the ultimate and failure strengths can be determined. The serpentine materials tested range in strength from 22.6 to 251.2 kPa and average 79.1 kPa. These values compare with an average of 29.1 kPa and a range of 16.0 to 51.0 kPa at Site 783 and an average of 11.6 kPa and a range of 1.3 to 38.0 kPa at Site 780 on the summit of Conical Seamount. Even excluding the anomalously strong, sheared, phacoidal serpentine at 15 cm in Section 125-784A-40R-2 (failure strength of 251.2 kPa), the average strength of the muds at Site 784 is 54.5 kPa, higher than the maximum strengths at other sites.

We postulate that the strength of these materials is related to their state of dewatering and lithification. This in turn is probably related to their age (older than middle Miocene, which is certainly older than the Site 780 sediments and flows and may be older than those at Site 783) and their depth of burial (340–370 mbsf, compared with 130–150 mbsf at Site 783 and 0–31 mbsf at Site 780). Thus, the strength data from Site 784 are consistent with a model in which serpentine mudflows are dewatering and compacting on the flanks of serpentinite seamounts.

PALEOMAGNETISM

Magnetic Remanence

We have identified many intervals of normal and reversed polarity in Hole 784A. These data, combined with the biostratigraphic data ("Biostratigraphy" section, this chapter), have enabled us tentatively to correlate a magnetostratigraphy

Table 9. Stress measurements of serpentine material recovered at Site 784.

Core, section	Depth (mbsf)	Stress (kPa)
125-784A-		
Sediments		
3R-1	11.81	19.7
3R-3	14.71	43.0
4R-3	24.22	34.9
6R-1	40.40	17.5
6R-3	43.33	29.8
6R-5	46.63	37.9
7R-1	50.08	34.9
7R-3	52.82	18.9
8R-2	60.88	52.4
8R-4	63.94	40.0
9R-2	70.90	32.0
9R-4	73.50	40.0
10R-2	80.20	25.5
10R-4	83.40	24.0
12R-2	99.38	57.5
13R-1	107.46	17.5
14R-2	118.78	54.6
14R-4	121.56	57.5
15R-2	128.75	54.6
15R-4	131.65	72.8
16R-1	137.00	43.0
16R-3	139.82	49.5
16R-5	142.91	57.5
17R-3	149.55	52.4
17R-5	152.60	85.9
Serpentine material		
37R-1	339.35	32.0
37R-1	339.92	22.6
37R-2	340.50	83.0
39R-2	360.35	52.4
40R-1	368.11	35.7
40R-1	368.59	72.1
40R-1	368.65	83.7
40R-2	369.15	251.2

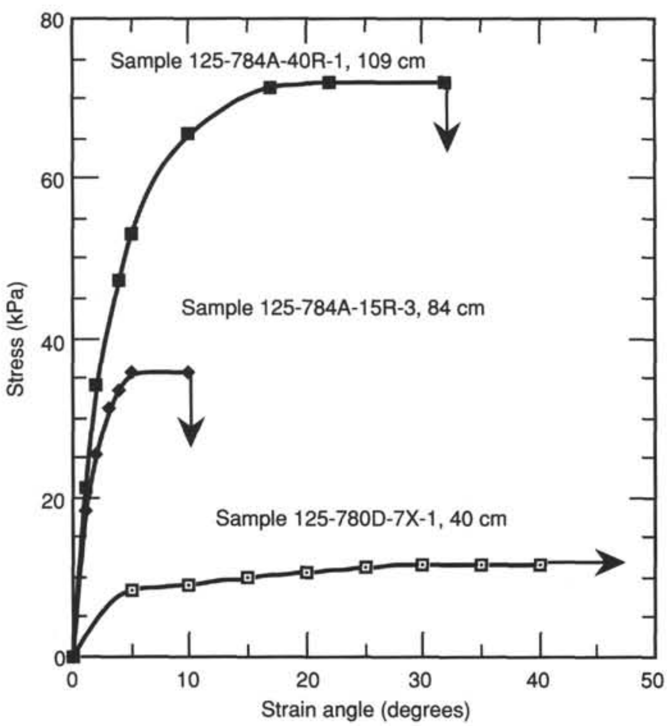

Figure 17. A representative stress-strain test of serpentine material from Site 784 (failure strength = 72.1 kPa), compared with those from Sites 780 (ultimate strength = 11.7 kPa) and 783 (failure strength = 35.7 kPa).

for the sediments in the upper 190-m section of Hole 784A (Fig. 18). However, a precise correlation with the magnetic time scale is impossible because of the lack of biostratigraphic data, the relatively poor magnetic data below 190 mbsf, and structural complications (beds dip at approximately 35° or greater). The natural remanent magnetization (NRM) of the archive half of each core from Hole 784A was measured using the cryogenic magnetometer. Magnetic intensities vary widely, from 1 to 800 mA/m (Fig. 19); most cores have values between 10 and 100 mA/m. At around 310 mbsf (Core 125-784A-34R), magnetic intensities increase, as does the amount of serpentine in the cores. When the cores were then demagnetized at the 10-mT level and remeasured, intensities were about 10% to 50% of their initial values. Some of the cores show signs of significant drilling disturbance. Data from cores described as more than slightly disturbed were rejected from any analysis.

Unfortunately, the biostratigraphic data, which are based almost entirely on the study of material from the core catchers (see "Biostratigraphy" section), are rather poor. A limited diatom zonation allows us to correlate tentatively the polarity sequence with the time scale of Berggren et al. (1985). Barron (1985) correlated the internationally recognized low-latitude diatom zones with the polarity time scale of Ness et al. (1980). At least for the interval from 0 to 11 Ma, the ages of each magnetochron boundary in that time scale are not appreciably different from those presented by Berggren et al. (1985). For practical purposes, the relative positions of the diatom zones of Barron (1985) can be transferred directly onto the time scale of Berggren et al. (1985). This modified scheme has been adopted for the present study. The magnetostratigraphy of the upper 190-m section of Hole 784A is summarized in Figure 18. However, the poor paleomagnetic and biostratigraphic data for Hole 784A make any accurate magnetostatigraphic correlation impossible.

Previous research on drill cores from the Philippine Sea Plate (Bleil, 1982) suggests that the Philippine Sea Plate has moved northward with time. The inclination data from Hole 784A were separated into 80-m sections, grouped into 10° intervals, and plotted on histograms (Fig. 20). The data from the intervals between 0 and 80 mbsf and between 80 and 160 mbsf show good bimodal distributions with peaks at about +50° and 50°. These data suggest little or no translation since the Pliocene. In the interval between 160 and 240 mbsf, there is no good bimodal distribution. Rather, the data are skewed to the positive side, suggesting that some material from this interval was remagnetized in the present field. However, there is a significant amount of data between +15° and 15°, which implies significant translation between the Miocene and Pliocene. Further research will be necessary to determine whether these low inclinations are merely a manifestation of insufficient cleaning of the overprint from the present field. In the interval between 240 and 312 mbsf, the distribution is dominated by positive inclination, with only a small percentage of the measurements showing negative inclination. This suggests that almost all of the rocks below 240 mbsf experienced recent remagnetization, possibly from the serpentization of the underlying rocks or by recent tectonic deformation.

Magnetic Susceptibility

Whole-core magnetic susceptibilities were measured using the multisensor track (MST). A downhole plot of these data for Hole 784A is presented in Figure 21. The sediments between 0 and 310 mbsf have values typically between 0 and 6×10^{-3} SI units. However, at the sediment/serpentine contact, there is a large increase in susceptibility to values between 12×10^{-3} and 48×10^{-3} SI units; this also

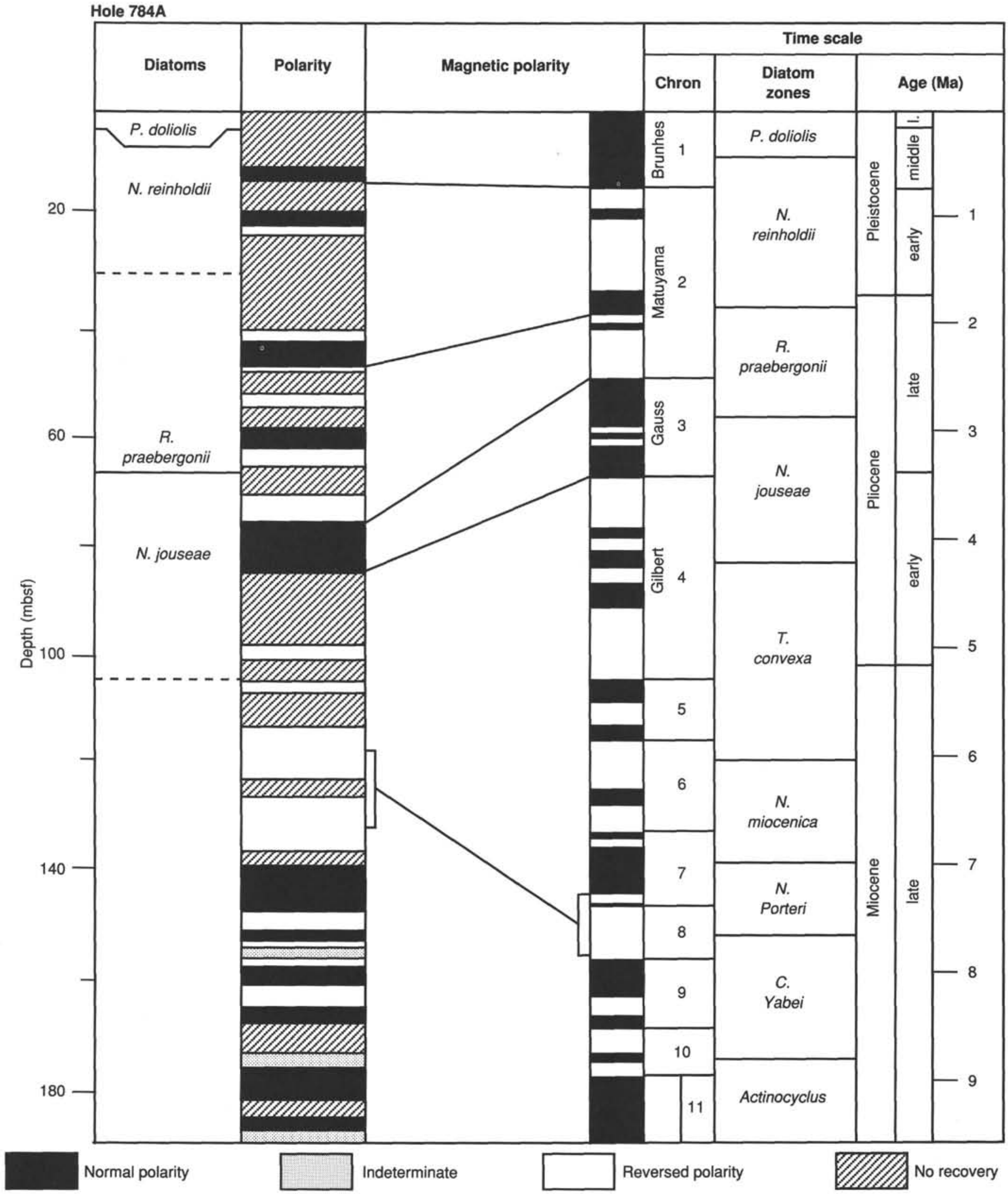

Figure 18. The magnetostratigraphy of Hole 784A for the interval from 0 to 190 mbsf, correlated with the polarity time scale of Berggren et al. (1985) and diatom zones modified from Barron (1985).

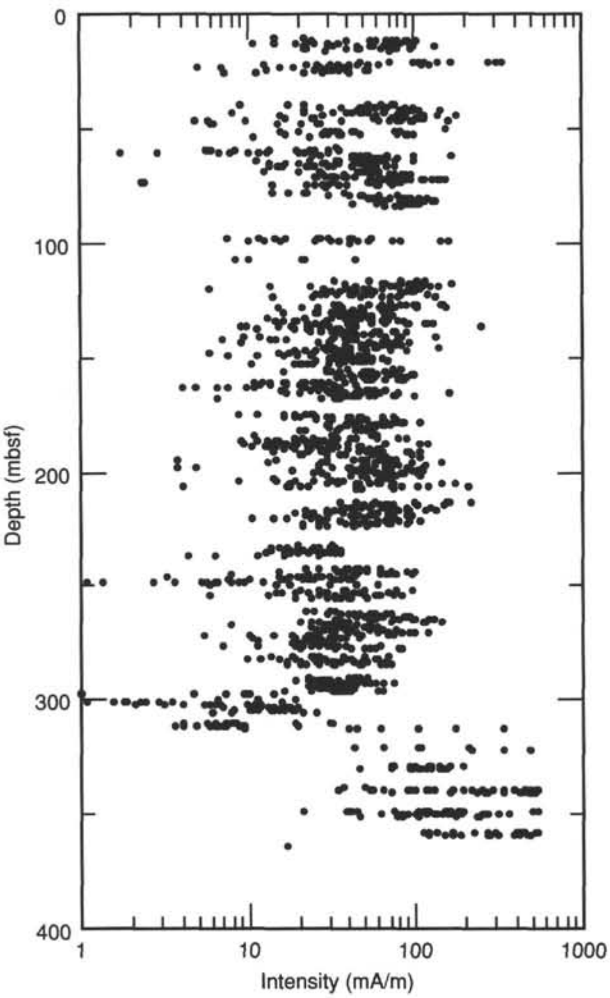

Figure 19. A downhole plot of magnetic intensity for Hole 784A.

correlates with an increase in magnetic intensity. The high magnetic susceptibility (and NRM intensity) associated with the serpentine probably results from the production of magnetite during the serpentinization process.

PHYSICAL PROPERTIES

The MST was used to determine bulk density (using the GRAPE), sonic velocity, and magnetic susceptibility of each core section from Hole 784A. Representative samples were selected from each section for measuring bulk density, grain density, porosity, water content, and thermal conductivity. Where possible, shear strength, resistivity, and sonic velocity (using the Hamilton Frame apparatus) were determined. The physical-properties data for Site 784 are listed in Tables 10 and 11 and plotted vs. depth in Figure 22.

A total of 300 m of volcaniclastic and pelagic sedimentary rocks was cored in Hole 784A. At about 300 mbsf, the serpentine sediment and flows and serpentinite clasts of Unit II were encountered. The physical properties of the volcaniclastic and pelagic sediment are distinct from those of the serpentine and serpentinite in Hole 784A. The average bulk density (as measured by the GRAPE) of the volcaniclastic and pelagic sediment is 1.56 ± 0.11 g/cm^3; that of the serpentine and serpentinite is 1.90 ± 0.23 g/cm^3.

Measurements of discrete samples show that the average bulk densities agree closely with the density values determined by the GRAPE. The average bulk density of the discrete samples of volcaniclastic and pelagic sediment is 1.57 ± 0.09 g/cm^3; that of the serpentine and serpentinite is 2.13 ± 0.37 g/cm^3. Bulk density increases slightly with depth in the sedimentary section and also increases with depth in the serpentine and serpentinite; however, the data are somewhat scattered, which results in a gradient of 0.0032 (Fig. 22). The average grain density, which is constant with depth, is 2.6± 0.17 g/cm^3 in the sediment and 2.70 ± 0.30 g/cm^3 in the serpentine and serpentinite.

The average thermal conductivity of the sediment is 0.914 ± 0.142 W/mK and increases with depth from 0.9 W/mK near the seafloor to 1.0 W/mK at about 310 mbsf (Fig. 22). Between 310 and 400 mbsf, thermal conductivity increases sharply from 1.2 to about 2.0 W/mK, resulting in a gradient of 0.003 in the serpentine and serpentinite.

Strength was measured in sections of sediment that were elastic enough to allow insertion of a shear vane. The sedimentary sections were measured to 150 mbsf, after which the sediment became too brittle to measure. Ultimate strength increases with depth in the sedimentary section from about 20 kPa near the seafloor to 80 kPa at 150 mbsf. Strength was measured in serpentinite from 340 to 370 mbsf. The values of ultimate strength in the serpentinite are scattered and range from 22.0 to 132.0 kPa, with one anomalous data point at 251.0 kPa. The stress-strain relationship of materials from Hole 784A is discussed in more detail in the "Structural Studies" section (this chapter).

The A and B directions of sonic velocity were measured with the Hamilton Frame apparatus (Fig. 22). The A velocity direction is parallel to the surface of the split core and the B velocity direction is perpendicular to the surface of the split core. The A and B velocities in sediment increase with depth from approximately 1600 m/s at 150 mbsf to 1750 m/s at 300 mbsf, resulting in gradients of 0.0016 and 0.0018, respectively. The average of both sonic velocities for sediment is 1670 m/s. However, the velocities from serpentine and serpentinite are widely scattered. The velocity measured in the A direction of serpentine and serpentinite is 1700 to 5700 m/s, and the B direction is from 1700 to 5400 m/s.

DOWNHOLE MEASUREMENTS

Three downhole temperature measurements were obtained at Site 784 using the Barnes-Uyeda temperature tool.

The temperature record from Run 05R at 29.9 mbsf is shown in Figure 23A and at an expanded scale in Figure 23B. The probemoved somewhat after emplacement, but was firmly seated in the sediment at 68 min into the run and remained relatively undisturbed until 80 min. After the first few minutes of emplacement, the temperature decay curve is proportional to 1/time. A linear least-squares regression on the curve, extrapolated to 1/time = 0, is a good estimate of the equilibrium sediment temperature, giving a value of 2.79°C, with a correlation coefficient (r^2) of 0.656 (Fig. 24). This temperature estimate may be somewhat high because of motion just after emplacement.

The temperature record from Run 11R at 107.1 mbsf is shown in Figure 25A and at an expanded scale in Figure 25B. The probe was seated in the sediment from 48 to 63 min into the run and has a clear cooling curve. The equilibrium temperature estimated from the decay curve is 4.62°C (Fig. 26); the r^2 value of 0.973 is high. The final temperature record from Run 17R at 145.6 mbsf is shown in Figure 27A and at an expanded scale in Figure 27B. The probe was in the sediment from 51 to 65 min with very little disturbance. The equilibrium temperature estimated from the decay curve is 5.46°C (Fig.

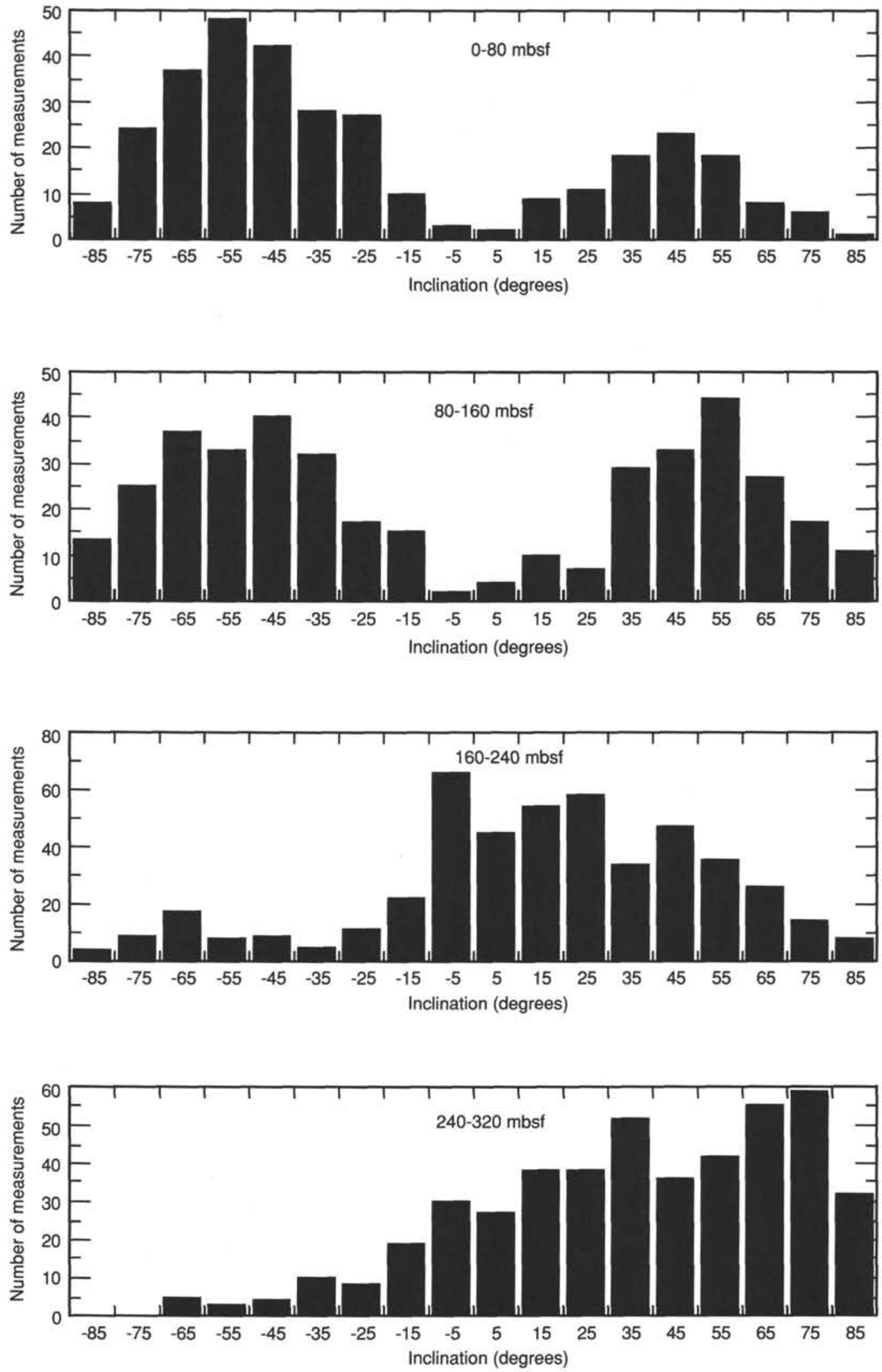

Figure 20. Inclination distribution as a function of depth, Hole 784A.

Table 10 . Index properties from Hole 784A.

Core, section, interval (cm)	Depth (mbsf)	Bulk density (g/cm^3)	Grain density (g/cm^3)	Porosity (%)	Water content (%)	Void ratio
125-784A-						
1R-1, 74–76	0.74	1.53	2.54	66.9	46.4	0.67
1R-CC, 22–24	1.16	1.59	2.63	65.5	43.8	0.66
2R-1, 5–7	1.45	1.51	2.42	66	46.6	0.66
3R-1, 74–76	11.64	1.46	2.48	70.4	51.2	0.7
3R-2, 35–37	12.75	1.51	2.3	62.9	44.3	0.63
3R-3, 67–69	14.57	1.51	2.65	70.8	49.8	0.71
3R-4, 18–20	15.58	1.38	1.98	63.6	49.1	0.64
4R-1, 31–33	20.71	1.44	2.53	73	53.8	0.73
4R-2, 31–33	22.21	1.55	2.81	70.9	48.4	0.71
4R-3, 31–33	23.71	1.47	2.66	73.3	53	0.73
4R-4, 31–33	25.21	1.55	2.55	66.3	45.5	0.66
6R-1, 76–78	40.26	1.49	2.45	68.2	48.7	0.68
6R-2, 80–82	41.8	1.46	2.53	71.5	52	0.72
6R-3, 85–87	43.35	1.42	2.59	75.3	56.2	0.75
6R-4, 90–92	44.9	1.49	2.6	71	50.6	0.71
6R-5, 91–93	46.41	1.57	2.63	66.5	45	0.67
6R-6, 45–47	47.45	1.52	2.61	69.3	48.4	0.69
7R-1, 67–69	49.77	1.54	2.59	67.8	46.8	0.68
7R-2, 65–67	51.25	1.49	2.68	72.3	51.4	0.72
7R-3, 65–67	52.75	1.54	2.87	72.6	50.1	0.73
8R-1, 69–71	59.49	1.46	2.53	71.7	52.3	0.72
8R-2, 106–108	61.36	1.56	2.79	70.1	47.7	0.7
8R-3, 52–54	62.32	1.56	2.61	67	45.7	0.67
8R-4, 56–58	63.86	1.52	2.46	66	46.1	0.66
8R-5, 51–53	65.31	1.54	2.62	67	46.2	0.67
9R-1, 85–87	69.35	1.51	2.56	69	48.5	0.69
9R-2, 85–87	70.85	1.49	2.68	72.7	52	0.73
9R-3, 77–79	72.27	1.52	2.5	66.7	46.5	0.67
9R-4, 42–44	73.42	1.54	2.66	68.8	47.3	0.69
9R-5, 27–29	74.77	1.49	2.74	72.7	51.7	0.73
10R-1, 49–51	78.59	1.55	2.6	67.2	46.1	0.67
10R-2, 59–61	80.19	1.51	2.59	69.6	48.9	0.7
10R-3, 103–105	82.13	1.48	2.59	71.4	51.1	0.71
10R-4, 80–82	83.4	1.49	2.66	72.1	51.4	0.72
12R-1, 58–60	97.98	1.53	2.59	68.1	47.2	0.68
12R-2, 44–46	99.34	1.44	2.59	73.9	54.4	0.74
13R-1, 36–38	107.46	1.52	2.57	68.2	47.6	0.68
14R-1, 97–99	117.67	1.55	2.6	67.4	46.3	0.67
14R-3, 30–32	120	1.47	2.56	71.5	51.5	0.71
14R-4, 30–32	121.5	1.51	3.24	44.5	31.3	0.45
14R-5, 70–72	123.4	1.5	2.52	68.5	48.4	0.68
15R-1, 78–80	127.18	1.45	2.53	72.2	52.8	0.72
15R-2, 56–58	128.46	1.45	2.51	71.8	52.5	0.72
15R-3, 94–96	130.34	1.52	2.49	66.9	46.8	0.67
15R-4, 96–98	131.86	1.45	2.53	72.6	53.3	0.73
15R-5, 79–81	133.19	1.51	2.22	81.2	56.9	0.81
15R-6, 79–81	134.69	1.57	2.69	68.1	46.2	0.68
15R-7, 39–41	135.79	1.53	2.61	68.3	47.3	0.68
16R-1, 56–58	136.56	1.49	2.67	72.4	51.8	0.72
16R-2, 56–58	138.06	1.54	2.42	63.8	44	0.64
16R-3, 56–58	139.56	1.5	2.63	71	50.3	0.71
16R-4, 56–58	141.06	1.52	2.51	67.5	47.3	0.68
16R-5, 56–58	142.56	1.5	2.59	70.1	49.6	0.7
16R-6, 41–43	143.91	1.56	2.54	65	44.2	0.65
16R-7, 41–43	145.41	1.58	2.62	65.9	44.4	0.66
17R-1, 86–88	146.46	1.53	2.66	69.5	48.2	0.7
17R-2, 48–50	147.58	1.53	2.5	66.2	45.9	0.66
17R-3, 51–53	149.11	1.52	2.54	68	47.6	0.68
17R-4, 51–53	150.61	1.51	2.59	69.5	48.8	0.69
17R-5, 34–36	151.94	1.49	2.57	70.4	50.1	0.7
18R-1, 90–92	156.2	1.54	2.5	66.1	45.7	0.66
18R-2, 121–123	158.01	1.58	2.73	67.8	45.5	0.68
18R-3, 105–107	159.35	1.56	2.54	65.4	44.6	0.65
18R-4, 82–84	160.62	1.58	2.5	62.9	42.4	0.63
18R-5, 118–120	162.48	1.47	2.61	72.8	52.7	0.73
18R-6, 18–20	162.98	1.5	2.55	69.2	49	0.69
18R-6, 86–88	163.66	1.53	2.57	68	47.3	0.68
19R-1, 56–58	165.56	1.6	2.5	61.4	40.7	0.61
19R-2, 36–38	166.86	1.67	2.51	56.8	36.1	0.57
20R-1, 104–106	175.74	1.58	2.51	63.1	42.4	0.63
20R-2, 120–121	177.4	1.58	2.88	65.9	44.4	0.66
20R-3, 109–111	178.79	1.59	2.63	65.3	43.7	0.65
20R-4, 48–49	179.68	1.75	2.83	60.1	36.4	0.6
20R-5, 56–58	181.26	1.62	2.71	65.1	42.6	0.65
21R-1, 108–110	185.48	1.42	2.63	52.9	39.5	0.53
21R-2, 65–67	186.55	1.69	2.8	62.9	39.5	0.63
21R-3, 21–23	187.61	1.62	2.7	65.2	42.8	0.65

Table 10 (continued).

Core, section, interval (cm)	Depth (mbsf)	Bulk density (g/cm^3)	Grain density (g/cm^3)	Porosity (%)	Water content (%)	Void ratio
21R-4, 106–108	189.96	1.73	2.85	61.8	38	0.62
21R-5, 18–20	190.58	1.62	2.89	68.6	45	0.69
22R-1, 96–98	194.96	1.61	2.9	69.2	45.6	0.69
22R-2, 96–98	196.46	1.64	2.91	67.7	43.7	0.68
22R-3, 124–126	198.24	1.58	2.81	69.6	46.8	0.7
22R-4, 114–116	199.64	1.62	2.87	68.4	45	0.68
22R-5, 67–69	200.67	1.65	2.96	68.1	43.8	0.68
22R-6, 66–68	202.16	1.6	2.73	67.2	44.7	0.67
23R-1, 133–135	204.93	1.66	2.74	63.7	40.8	0.64
23R-2, 104–106	206.14	1.51	2.5	68.3	48	0.68
23R-3, 30–32	206.9	1.63	2.78	66	43	0.66
24R-1, 34–36	213.54	1.56	2.76	69.9	47.7	0.7
24R-2, 41–43	215.11	1.5	2.69	72.3	51.3	0.72
24R-3, 110–112	217.3	1.57	2.74	69	46.7	0.69
24R-4, 127–129	218.97	1.49	2.55	70	49.8	0.7
24R-5, 29–31	219.49	1.53	2.69	70.1	48.6	0.7
24R-6, 18–20	220.88	1.58	2.88	70.5	47.3	0.7
25R-1, 59–61	223.49	1.6	2.58	63.6	42.2	0.64
26R-1, 95–97	233.45	1.53	2.79	72.1	50.1	0.72
26R-2, 40–42	234.4	1.56	2.66	68.1	46.5	0.68
27R-1, 117–119	243.27	1.6	2.58	63.3	41.9	0.63
27R-2, 104–106	244.64	1.72	2.85	62.2	38.3	0.62
27R-3, 82–84	245.92	1.79	2.79	57.5	34.2	0.57
27R-4, 53–55	247.13	1.57	2.57	65	43.9	0.65
27R-5, 80–82	248.9	1.61	2.55	63.8	42.2	0.64
28R-1, 110–112	252.9	1.56	2.58	66	44.9	0.66
28R-2, 86–88	254.16	1.68	2.75	62.4	39.3	0.62
28R-3, 21–23	255.01	1.63	2.57	61.1	39.7	0.61
29R-1, 99–101	262.39	1.73	2.79	60.4	37.1	0.6
29R-2, 107–109	263.97	1.74	2.46	56.2	34.2	0.56
29R-3, 57–59	264.97	1.7	2.81	62.7	39.2	0.63
29R-4, 49–51	266.39	1.69	2.82	63.7	40.2	0.64
29R-5, 55–57	267.95	1.64	2.75	64.8	42	0.65
29R-6, 28–30	269.18	1.68	2.95	66.5	42.1	0.67
29R-7, 39–41	270.79	1.74	2.65	56.7	34.7	0.57
30R-1, 34–36	271.44	1.72	2.71	59.1	36.4	0.59
30R-2, 93–95	273.53	1.61	2.53	61.7	40.8	0.62
30R-3, 82–84	274.92	1.71	2.73	60.4	37.6	0.6
30R-4, 69–72	276.29	1.66	2.67	62	39.7	0.62
30R-5, 48–50	277.58	1.72	2.66	57.9	35.8	0.58
31R-1, 31–34	281.11	1.74	2.94	63.2	38.6	0.63
31R-2, 83–86	283.13	1.7	2.64	58.8	36.8	0.59
31R-3, 81–83	284.61	1.72	2.72	59.5	36.8	0.6
32R-1, 86–88	291.26	1.72	2.87	62.8	38.8	0.63
32R-2, 99–101	292.89	1.66	2.84	65.5	41.9	0.66
32R-3, 70–72	294.1	1.69	2.86	64	40.1	0.64
32R-4, 43–45	295.33	1.75	3.1	65.3	39.6	0.65
32R-5, 24–26	296.64	1.67	2.99	67.7	43.1	0.68
32R-6, 112–114	299.02	1.6	2.94	70.7	47	0.71
32R-7, 33–35	299.73	1.54	2.78	70.9	48.8	0.71
33R-1, 33–34	300.33	1.53	2.8	71.9	49.8	0.72
33R-2, 122–123	302.72	1.73	2.74	63.1	38.8	0.63
33R-3, 55–56	303.55	1.85	2.8	53.9	30.9	0.54
33R-4, 50–52	305	1.89	2.54	62.2	34.9	0.62
34R-1, 11–13	309.81	1.91	2.8	50.4	28	0.5
34R-2, 31–33	311.51	1.77	2.63	54.1	32.6	0.54
35R-1, 131–133	320.61	1.98	2.71	43.9	23.6	0.44
35R-2, 22–24	321.02	2.03	2.78	43.4	22.7	0.43
36R-1, 33–35	329.33	1.71	2.57	37.9	23.5	0.38
36R-1, 107–109	330.07	2.39	2.57	11.4	5.1	0.11
37R-1, 71–73	339.41	1.99	2.61	39.4	21	0.39
38R-1, 66–68	348.96	3.55	4.02	15.8	4.7	0.16
38R-2, 29–31	350.09	2.05	2.64	36.8	19.1	0.37
39R-1, 80–82	358.7	2.1	2.66	34.5	17.4	0.34
39R-2, 83–85	360.23	2.09	2.62	33.4	17	0.33
40R-1, 94–97	368.44	2.08	2.8	40.9	20.9	0.41
40R-2, 41–43	369.41	2.48	2.51	2.3	1	0.02
41R-1, 70–72	378	1.81	2.51	47.2	27.6	0.47
41R-2, 98–100	379.35	2.09	2.38	21.6	11	0.22
42R-1, 39–41	387.29	2.34	2.58	15.1	6.8	0.15
42R-1, 80–82	387.7	1.93	2.64	44.1	24.2	0.44
42R-2, 41–43	388.81	1.94	2.67	44.7	24.5	0.45
43R-1, 103–105	397.63	2.01	2.67	40.2	21.2	0.4
43R-2, 98–100	399.08	2.12	2.76	36.9	18.5	0.37
43R-3, 60–62	400.2	2.06	2.79	41.7	21.5	0.42
45R-1, 98–100	416.58	2.68	2.69	0.5	0.2	0
45R-2, 92–94	418.02	2.35	2.51	11	5	0.11

Table 11. Physical properties from Hole 784A.

Core, section, interval (cm)	Depth (mbsf)	Thermal conductivity (W/mK)	Ultimate strength (kPa)	Resistivity (ohms)	Formation factor	Compressional-wave velocity A direction (km/s)	Compressional-wave velocity B direction (km/s)
125-784A-							
1R-1, 76	0.76	0.851					
1R-CC, 22	1.16	0.99					
2R-1, 5–13	1.53	0.968		12.6	1.47		
3R-1, 10–14	11.02			13.9	1.62		
3R-1, 10–14	11.02			13.6	1.59		
3R-1, 33	11.23	0.729					
3R-1, 91–93	11.81		19.7				
3R-2, 33	12.73	0.894					
3R-3, 33	14.23	0.936					
3R-3, 81–83	14.71		43				
3R-4, 33	15.73	0.907					
4R-1, 15–19	20.57			14.9	1.74		
4R-1, 49	20.89	1.011					
4R-2, 49	22.39	0.936					
4R-3, 10–14	23.52			15.2	1.77		
4R-3, 49	23.89	1.01					
4R-3, 82–84	24.22		34.9				
4R-4, 49	25.39	0.963					
6R-1, 30–34	39.82			16.9	1.97		
6R-1, 65	40.15	1.015					
6R-1, 90–91	40.4		17.5				
6R-2, 65	41.65	1.247					
6R-3, 20–24	42.72			17.3	2.02		
6R-3, 65	43.15	0.948					
6R-3, 83–85	43.33		29.8				
6R-4, 65	44.65	0.981					
6R-5, 10–14	45.62			16.5	1.93		
6R-5, 46	45.96	0.899					
6R-5, 113–115	46.63		37.9				
6R-6, 46	47.46	0.957					
7R-1, 74	49.84	0.921					
7R-1, 106–110	50.18		34.9	16.1	1.88		
7R-2, 40–44	51.02			16.6	1.94		
7R-2, 74	51.34	0.852					
7R-3, 60–64	52.72		18.9	15.4	1.8		
7R-3, 74	52.84	1.03					
8R-1, 40–44	59.22			19	2.22		
8R-1, 70	59.5	0.9					
8R-2, 58–60	60.88		52.4				
8R-2, 70	61	0.864					
8R-3, 46–48	62.28			17.4	2.03		
8R-3, 70	62.5	0.971					
8R-4, 64–66	63.94		40				
8R-4, 70	64	0.93					
8R-5, 54–58	65.36			16	1.87		
8R-5, 59–63	65.41			18.5	2.16		
8R-5, 21	65.01	0.784					
8R-6, 21	66.51	0.963					
9R-1, 75	69.25	0.796					
9R-1, 90–94	69.42			16.5	1.93		
9R-2, 75	70.75	0.705					
9R-2, 90–92	70.9		32				
9R-3, 75	72.25	1.021		18.5	2.16		
9R-4, 50–52	73.5		40				
9R-4, 75	73.75	0.951					
9R-5, 20–24	74.72			19.5	2.28		
9R-5, 37	74.87	1.005					
9R-CC, 6	75.33	0.838					
10R-1, 52	78.62	0.931		17.5	2.04		
10R-2, 60–62	80.2		25.5				
10R-2, 75	80.35	0.936					
10R-3, 75	81.85	0.918					
10R-3, 100–104	82.12			17	1.98		
10R-4, 60	83.2	0.915					
10R-4, 80–82	83.4		24				
10R-5, 6–10	83.5			24.5	2.86		
10R-CC, 6	83.86	0.876					
11R-CC, 9	87.89	0.795					
12R-1, 56–60	97.98			17	1.98		
12R-1, 75	98.15	0.921					
12R-1, 104–108	98.46			19	2.22		
12R-2, 41	99.31	0.976	57.5				
13R-1, 29–34	107.39	0.909		18	2.1		
13R-1, 38–42	107.5		17.5	19	2.22		

Table 11 (continued).

Core, section, interval (cm)	Depth (mbsf)	Thermal conductivity (W/mK)	Ultimate strength (kPa)	Resistivity (ohms)	Formation factor	Compressional-wave velocity A direction (km/s)	Compressional-wave velocity B direction (km/s)
13R-1, 38–42	107.5			21	2.45		
13R-1, 42–46	107.54			22	2.57		
14R-1, 80	117.5	0.951					
14R-1, 96–100	117.68			15.5	1.81		
14R-2, 58–60	118.78		54.6				
14R-2, 74	118.94	0.787					
14R-3, 28–32	120			17	1.98		
14R-3, 56	120.26	0.949					
14R-4, 36–38	121.56		57.5				
14R-4, 72	121.92	0.95					
14R-5, 49	123.19	0.969					
14R-5, 64–66	123.26			18.5	2.16		
14R-CC, 10	123.78	0.996					
15R-1, 75	127.15	0.912					
15R-2, 75	128.65	0.979					
15R-2, 85–87	128.75		54.6				
15R-2, 96–100	128.88			18	2.1		
15R-3, 50–54	129.92			15.5	1.81		
15R-3, 75	130.15	0.946					
15R-4, 75–77	131.65	0.858	72.8				
15R-4, 100–104	131.92			19	2.22		
15R-5, 75	133.15	0.947					
15R-6, 75	134.65	0.838					
15R-7, 30	135.7	0.991					
15R-CC, 10	136.11	0.852		24.9	2.91		
16R-1, 75	136.75	0.792					
16R-1, 100–102	137		43				
16R-2, 75	138.25	0.971					
16R-3, 10–14	139.12			19.3	2.25		
16R-3, 75	139.75	0.952	49.5				
16R-4, 75	141.25	0.989					
16R-5, 13–17	142.15			22.6	2.64		
16R-5, 75	142.75	0.801					
16R-5, 91–93	142.91		57.5				
16R-6, 75	144.25	0.995					
16R-7, 10–14	145.12			29.4	3.43		
16R-7, 29	145.29	0.916					
16R-CC, 10	145.7	0.906					
17R-1, 12–16	145.74			24.9	2.91		
17R-1, 75	146.35	0.958					
17R-2, 75	147.85	0.961					
17R-3, 17–21	148.79			23.3	2.72		
17R-3, 75	149.35	0.968					
17R-3, 95–97	149.55		52.4				
17R-4, 75	150.85	0.908					
17R-5, 5–9	151.67			26.9	3.14		
17R-5, 64	152.24	0.875					
17R-5, 100–102	152.6		85.9				
18R-1, 64	155.94	0.938					
18R-1, 90–92	156.2					1.6	1.63
18R-2, 64	157.44	0.985					
18R-3, 64	158.94	0.898					
18R-4, 38	160.18	0.788					
18R-5, 38	161.68	0.998					
18R-6, 38	163.18	0.973					
18R-7, 38	164.68	0.931					
19R-1, 91	165.91	0.952					
19R-2, 36–38	166.86					1.67	1.68
19R-2, 91	167.41	0.924					
20R-1, 54	175.24	0.963					
20R-1, 104–106	175.74					1.6	1.61
20R-2, 54	176.74	0.954					
20R-3, 54	178.24	0.952					
20R-4, 54	179.74	1.062					
20R-5, 44	181.14	0.924					
21R-1, 44	184.84	0.908					
21R-1, 108–110	185.48					1.69	1.68
21R-2, 44	186.34	0					
21R-2, 65–67	186.55					1.7	1.74
21R-2, 88	186.78	0.693					
21R-3, 21–23	187.61					1.62	1.62
21R-3, 44	187.84	1.048					
21R-4, 59	189.49	0.945					
21R-4, 106–108	189.96					1.64	1.63
21R-5, 18–20	190.58					1.57	1.58

Table 11 (continued).

Core, section, interval (cm)	Depth (mbsf)	Thermal conductivity (W/mK)	Ultimate strength (kPa)	Resistivity (ohms)	Formation factor	Compressional-wave velocity A direction (km/s)	Compressional-wave velocity B direction (km/s)
21R-5, 59	190.99	1.039					
21R-6, 59	192.49	0.907					
22R-1, 96–98	194.96					1.58	1.58
22R-2, 59	196.09	0.902					
22R-2, 96–98	196.46					1.58	1.6
22R-3, 80	197.8	1.001					
22R-3, 124–126	198.24					1.57	1.56
22R-4, 80	199.3	0.895					
22R-4, 114–116	199.64					1.57	1.61
22R-5, 67–69	200.67					1.56	1.58
22R-5, 80	200.8	1.027					
22R-6, 66–68	202.16					1.59	1.59
22R-6, 80	202.3	1.026					
23R-1, 54	204.14	1.031					
23R-1, 133–135	204.93					1.62	1.62
23R-2, 54	205.64	0.959					
23R-2, 104–106	206.14					1.58	1.59
23R-3, 54	207.14	0.951					
24R-1, 34–36	213.54					1.58	1.6
24R-1, 81	214.01	0.847					
24R-2, 41–43	215.11					1.57	1.55
24R-2, 81	215.51	0.924					
24R-3, 81	217.01	1.009					
24R-3, 110–112	217.3					1.6	1.6
24R-4, 81	218.51	1.008					
24R-4, 127–129	218.97					1.59	1.58
24R-5, 31	219.51	0.951				1.57	1.56
24R-6, 18–20	220.88					1.58	1.59
24R-6, 31	221.01	0.93					
24R-7, 31	222.51	0.979					
25R-1, 31	223.21	0.774					
25R-1, 59–61	223.49					1.62	1.63
26R-1, 50	233	1.022					
26R-1, 95–97	233.45					1.57	1.59
26R-2, 40–42	234.4					1.58	1.59
26R-2, 68	234.68	0.945					
26R-3, 68	236.18	0.954					
27R-1, 93	243.03	0.955					
27R-1, 117–119	243.27					1.66	1.69
27R-2, 75	244.35	0.966					
27R-2, 104–106	244.64					1.73	1.76
27R-3, 75	245.85	0.965				1.75	1.85
27R-4, 53–55	247.13					1.61	1.64
27R-4, 75	247.35	1.002					
27R-5, 75	248.85	1.003				1.69	1.68
28R-1, 75	252.55	0.355					
28R-1, 110–112	252.9					1.6	1.61
28R-2, 75	254.05	1.002					
28R-2, 86–88	254.16					1.67	1.67
28R-3, 22	255.02	1.018					
28R-3, 99–101	255.8					1.68	1.74
29R-1, 21–23	261.61					1.77	1.88
29R-1, 75	262.15	0.768					
29R-2, 75	263.65	0.979					
29R-2, 107–109	263.97					1.88	1.88
29R-3, 57–59	264.97					1.74	1.74
29R-3, 75	265.15	0.92					
29R-4, 52	266.42	0.545				1.72	1.73
29R-5, 55–57	267.95					1.69	1.7
29R-5, 82	268.22	0.756					
29R-6, 28–30	269.18					1.67	1.67
29R-6, 82	269.72	1.016					
29R-7, 37–39	270.77	1.032				1.75	1.77
30R-1, 34–36	271.44					1.73	1.79
30R-1, 75	271.85	0.746					
30R-2, 75	273.35	0.934					
30R-3, 75	274.85	0.854					
30R-4, 69–75	276.35	0.971				1.78	1.76
30R-5, 41–43	277.49	0.249				1.76	1.83
31R-1, 31–33	281.11					1.84	
31R-1, 70	281.5	0.936					
31R-2, 68	282.98	1.083					
31R-3, 68	284.48	1.005					
31R-3, 81–83	284.61					1.75	
32R-1, 75	291.15	1.06					

Table 11 (continued).

Core, section, interval (cm)	Depth (mbsf)	Thermal conductivity (W/mK)	Ultimate strength (kPa)	Resistivity (ohms)	Formation factor	Compressional-wave velocity A direction (km/s)	Compressional-wave velocity B direction (km/s)
32R-1, 86–88	291.26					1.73	1.87
32R-2, 75	292.65	0.954					
32R-3, 75	294.15	0.945				1.79	1.79
32R-4, 43–45	295.33					1.82	1.81
32R-5, 24–26	296.64					1.74	1.76
32R-5, 73	297.13	0.705					
32R-6, 51	298.41	0.954					
32R-7, 32	299.72	0.691					
33R-1, 75	300.75	1.02					
33R-2, 75	302.25	1.405					
33R-3, 75	303.75	1.199					
33R-4, 47	304.97	1.234					
34R-1, 75	310.45	1.426					
34R-2, 75	311.95	1.11					
34R-CC, 6	312.91	1.27					
35R-1, 60	319.9	1.081					
35R-2, 22–24	321.02					1.96	2.33
35R-2, 49	321.29	1.705					
35R-CC, 5	321.78	1.496					
36R-1, 104–107	330.04	1.814				3.45	3.5
36R-1, 116–120	330.18			33.6	3.92		
36R-2, 10–14	330.62			41.1	4.8		
37R-1, 65–67	339.35		32				
37R-1, 99	339.69	0.89					
37R-1, 122–124	339.92		22.6				
37R-2, 27	340.47	2.03	83				
38R-1, 61–66	348.91	1.59				3.63	3.56
38R-2, 29–31	350.09					2.24	1.98
39R-1, 75	358.65	2.458	132.5				
39R-2, 70	360.1	2.983					
39R-2, 95–97	360.35		52.4				
40R-1, 61–64	368.14	2.568	35.7				
40R-1, 94–96	368.44					1.79	
40R-1, 109–111	368.59		72.1				
40R-1, 115–117	368.65		83.7				
40R-2, 15–17	369.15		251.2				
40R-2, 50–52	369.5					4.94	4.84
41R-2, 98–100	379.35					3.81	3.84
42R-1, 39–41	387.29					3.19	3.27
42R-2, 22	388.62	2.35					
43R-1, 96	397.56	1.895				1.74	1.7
43R-2, 47	398.57	2.05					
43R-2, 98–100	399.08					1.84	1.87
43R-3, 33	399.93	1.759					
43R-3, 60–62	400.2					1.74	1.7
45R-1, 83	416.43	1.751					
45R-1, 99–100	416.59					5.66	5.45
45R-2, 60	417.7	2.098					
45R-2, 92–94	418.02					3.82	3.78

28), with a low r^2 of 0.426. The slope of the decay curve is low, thus any errors should be minor.

Thermal-conductivity data are presented in Figure 29 (see "Physical Properties" section, this chapter). Temperatures were measured above the depth where a large increase in thermal conductivity occurs. The integrated thermal resistivity is shown in Figure 30.

The equilibrium temperature and integrated thermal resistivity data are plotted in Figure 31. The slope of the linear least-squares regression at this site gives a heat flow of 24 mW/m^2. The correlation coefficient for the fit is 0.988. The misfit of the data to the regression for the uppermost sediment measurement may be caused by the slight motion of the probe in the sediment, as previously mentioned.

SUMMARY AND CONCLUSIONS

Site 784, at 30°54.49′N, 141°44.27′E, in a water depth of 4900.8 m, is located approximately 7 km southwest of Site 783 on the lowermost, western flank of the same seamount on the inner wall of the Izu-Bonin Trench. The stratigraphic section recovered at Site 784 is divided into the three subunits of lithologic Unit I and a lithologic Unit II (Fig. 32): Subunit IA (0–126.4 mbsf) consists of vitric clayey silt, glass-rich silty clay/claystone of late Pleistocene to early Pliocene(?) age; Subunit IB (126.4–302.7 mbsf) is a vitric claystone of early Pliocene(?) to middle Miocene age; Subunit IC (302.7–321.1 mbsf) consists of claystone and silt-sized serpentine of unknown age; and Unit II (321.1–425.3 mbsf) is a phacoidal, sheared serpentine microbreccia.

Dating is based on calcareous nannofossil and diatom biostratigraphy. Lithologic Subunit IB may correlate with lithologic Subunit IB at Site 782 in the forearc basin on the basis of age and ash content, although there is a depleted carbonate/microfossil component at Site 784 because of sediment deposition at or below the CCD. Sediments from Subunits IA and IB at Site 784 are typically laminated and contain abundant graded beds, structures that are indicative of current activity during sediment deposition. The sediment contains a

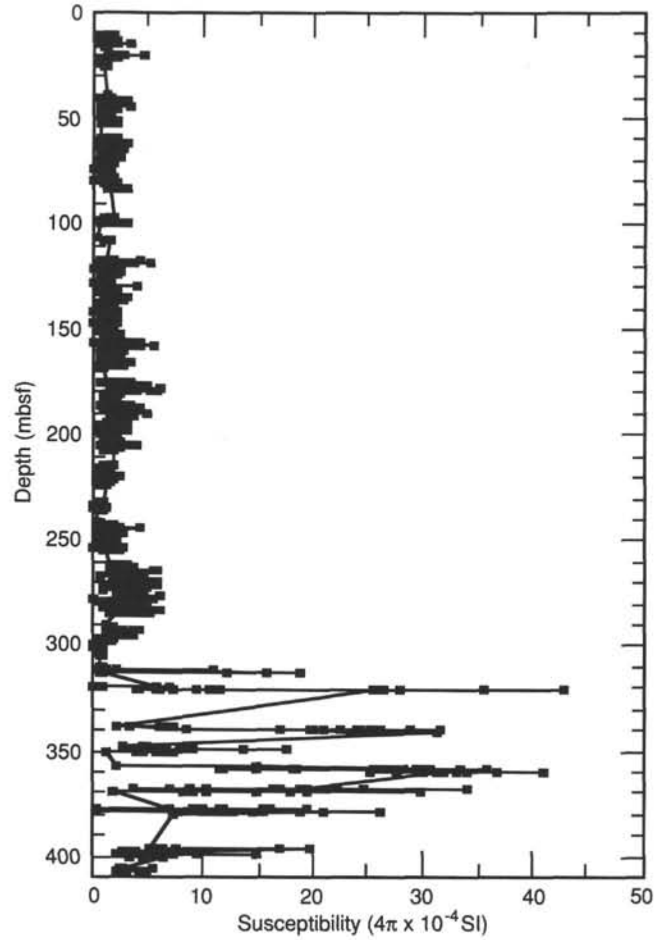

Figure 21. A downhole plot of susceptibility for Hole 784A.

high volcanogenic component and numerous ash layers typically made up of glass and feldspar with lesser amounts of pyroxenes, amphibole, opaque minerals, epidote group minerals, chlorite, and clays. Subunit IC shows a clear interfingering of background pelagic sediments derived from the volcanic areas to the west and silt-sized serpentine from the topographic high to the east.

The ultramafic clasts from Unit II are of two types: (1) variably serpentinized tectonized harzburgite consisting of olivine (70–90 modal%) and orthopyroxene (30–10 modal%) with minor clinopyroxene (as exsolution lamellae in orthopyroxene) and spinel and (2) subordinate dunites containing olivine (90%–99%), orthopyroxene (10%–1%), and spinel (0.5%–2%). About 30 metabasalt clasts were also identified.

Deformation in the claystones of Unit I at Site 784 includes sets of *en echelon* tension veinlets and sets of microfaults, some of which are clearly associated with water-escape pipes. The zone of greatest microfaulting is directly correlated with an interval of increased water content and porosity of the sediments. Most structures are extensional and can be shown to have formed in a nonhydrostatic stress regime. Unit II includes pebbly serpentines with convolute lamination, sheared and relatively unsheared, pebbly silt-sized serpentines without convolute lamination, and serpentine microbreccias. Some of these layers exhibit irregular size grading and many contain larger blocks, mostly of serpentinite.

Analyses of the interstitial waters show a steady change in composition with depth within the claystone, followed by an abrupt change in behavior at the claystone/serpentine boundary. As at Site 783, the most abrupt changes are in pH, which increases to 9.6 in the serpentine, and silica, which decreases to less than 10 μmol/kg. Other species showing a marked change in behavior are alkalinity, which decreases to a value about one-half that of seawater within the serpentine; sulfate, which decreases to 7 mmol/kg; calcium, which increases to 57 mmol/kg; and magnesium, which decreases to very low values. As at Site 783, chlorinity, bromide, and salinity show no major changes, but sodium decreases to 452 μmol/kg, in contrast to its behavior at Site 783. Thus, as at Site 783, there is evidence for ongoing serpentinization at the Torishima Forearc Seamount.

Studies of physical properties show that the average bulk densities are 1.5 g/cm^3 in the sediments of Unit I and 2.2 g/cm^3 in the serpentine of Unit II. The average compressional-wave velocity is 1.66 km/s in the sediments and 3.08 km/s in the serpentine and serpentinites. The thermal conductivity averages about 0.9 W/mK in the sediments and 1.74 W/mK in the serpentine and serpentinite.

Preliminary interpretation of paleomagnetic data from the sediments between 0 and 160 mbsf shows magnetic inclination peaks around +50° and 50°, indicating little translation since the Pliocene. In the interval between 160 and 240 mbsf, there is no good bimodal distribution and a significant number of data points lie between +15° and 15°, which suggests that a significant translation may have occurred between the middle Miocene and the Pliocene. No inclination data were obtained below 240 mbsf, but magnetic susceptibilities did increase markedly at the claystone/serpentine boundary, perhaps because the serpentine contains a high proportion of secondary magnetite.

The principal results of this site are (1) the confirmation that the western lower flank of the seamount is also made up of serpentine-rich sediments and serpentinite, (2) further biostratigraphic evidence that the serpentine sediment is at least middle Miocene and hence that the seamount is considerably older than Conical Seamount in the Mariana forearc, (3) the structural evidence for extensional deformation within the more compacted sediments overlying serpentine-rich sediments and serpentinite, (4) possible paleomagnetic evidence for significant translation of the site between middle Miocene and Pliocene, and (5) the evidence that serpentinization is still taking place, despite the lack of evidence for active protrusion.

REFERENCES

Arthur, M. A., Carson, B., and von Huene, R., 1980. Initial tectonic deformation of hemipelagic sediment at the leading edge of the Japan convergent margin. *In* Langseth, M., Okada, H., et al., *Init. Repts. DSDP*, 56, 57 (Pt. 1): Washington (U.S. Govt. Printing Office), 569–613.

Barron, J. A., 1985. Miocene to Holocene planktonic diatoms. *In* Bolli, H., Saunders, J. B., and Perch-Nielsen, K. (Eds.), *Plankton Stratigraphy*: Cambridge (Cambridge Univ. Press), 763–810.

Berggren, W. A., Kent, D. V., Flynn, J. J., and Van Couvering, J., 1985. Cenozoic geochronology. *Geol. Soc. Am. Bull.*, 96:1407–1418.

Bleil, U., 1982. Paleomagnetism of Deep Sea Drilling Project Leg 60 sediments and igneous rocks from the Mariana region. *In* Hussong, D. M., Uyeda, S., et al., *Init. Repts. DSDP*, 60: Washington (U.S. Govt. Printing Office), 855–873.

Cowan, D. S., 1982. Origin of "vein structure" in slope sediments on the inner slope of the Middle America Trench off Guatemala. *In* Aubouin, J., von Huene, R., et al., *Init. Repts. DSDP*, 67: Washington (U.S. Govt. Printing Office), 645–650.

Cowan, D. S., Moore, J. C., Roeske, S. M., Lundberg, N., and Lucas, S. E., 1984. Structural features at the deformation front of the Barbados Ridge complex, Deep Sea Drilling Project Leg 78A. *In* Biju-Duval, B., Moore, J. C., et al., *Init. Repts. DSDP*, 78A: Washington (U.S. Govt. Printing Office), 535–548.

Dengo, C. A., 1982. A structural analysis of cores from the Leg 67 transect across the Middle America Trench–offshore Guatemala. *In* Aubouin, J., von Huene, R., et al., *Init. Repts. DSDP*, 67: Washington (U.S. Govt. Printing Office), 651–666.

Kobayashi, K. (Ed.), 1989. *Preliminary Report of the Hakuho Maru Cruise KH-87-3, July-August 13, 1988, Izu-Ogasawara (Bonin), East Mariana Basin and Yap Trench (WESTPAC, ODP Site Survey)*: Tokyo (Ocean Research Institute, Univ. of Tokyo).

Ness, G., Levi, S., and Crouch, R., 1980. Marine magnetic anomaly time scales for the Cenozoic and Late Cretaceous. A précis, critique and synthesis. *Rev. Geophys. Space Phys.*, 198:753–770.

Ms 125A-112

NOTE: All core description forms ("barrel sheets") and core photographs have been printed on coated paper and bound as Section 4, near the back of the book, beginning on page 383.

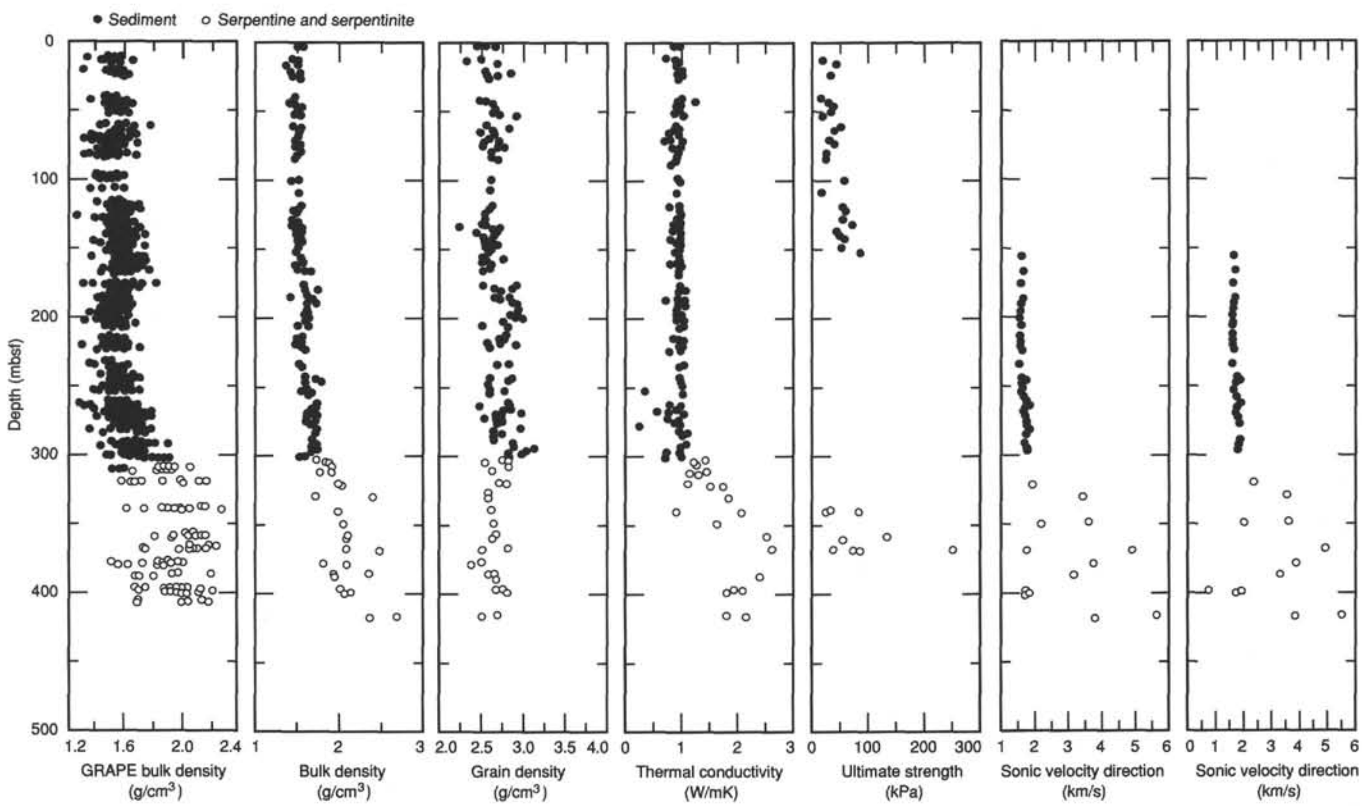

Figure 22. Bulk density (determined by the GRAPE and from discrete samples), grain density, thermal conductivity, ultimate strength, and A (parallel to the split-core surface) and B (perpendicular to the split-core surface) directions of sonic velocity.

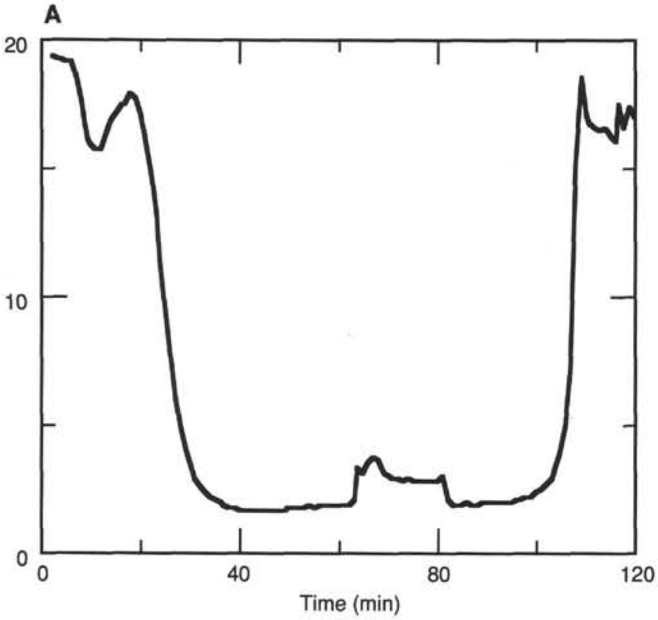

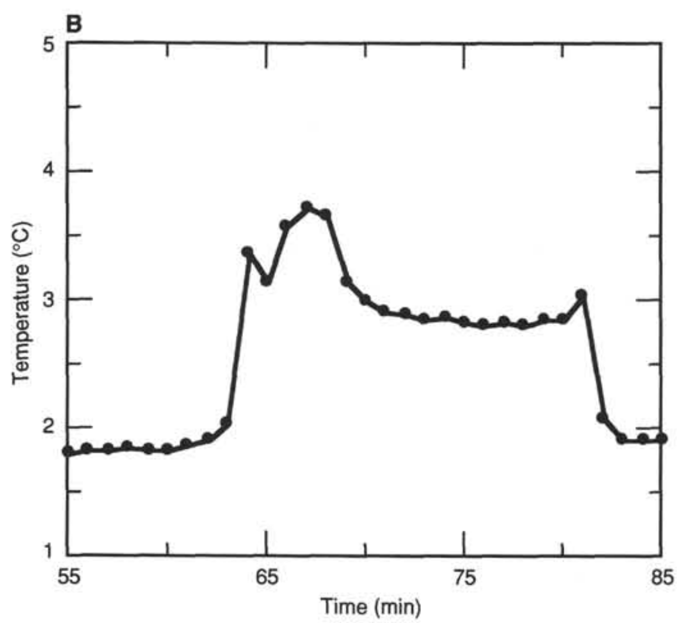

Figure 23. **A.** Temperature vs. time for Run 05R of the Barnes-Uyeda tool at 29.9 mbsf in Hole 784A. **B.** An expanded plot showing the data when the tool was in the seafloor. Note the disturbance of the probe from 65 to 67 min.

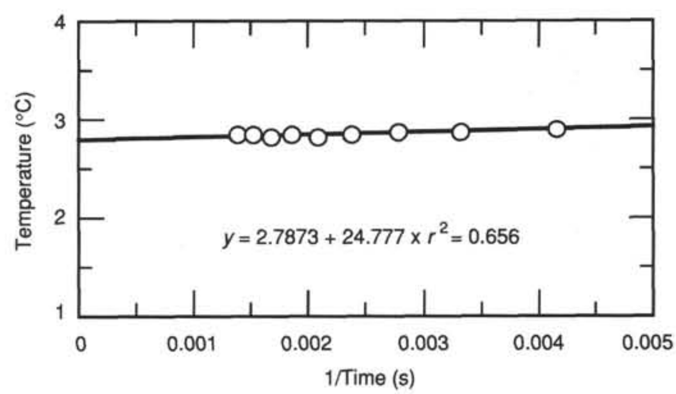

Figure 24. The reduced temperature fit of the first Barnes-Uyeda temperature run using data from the later portion of the run. The intercept value at 1/time = 0 is the equilibrium temperature of the sediment.

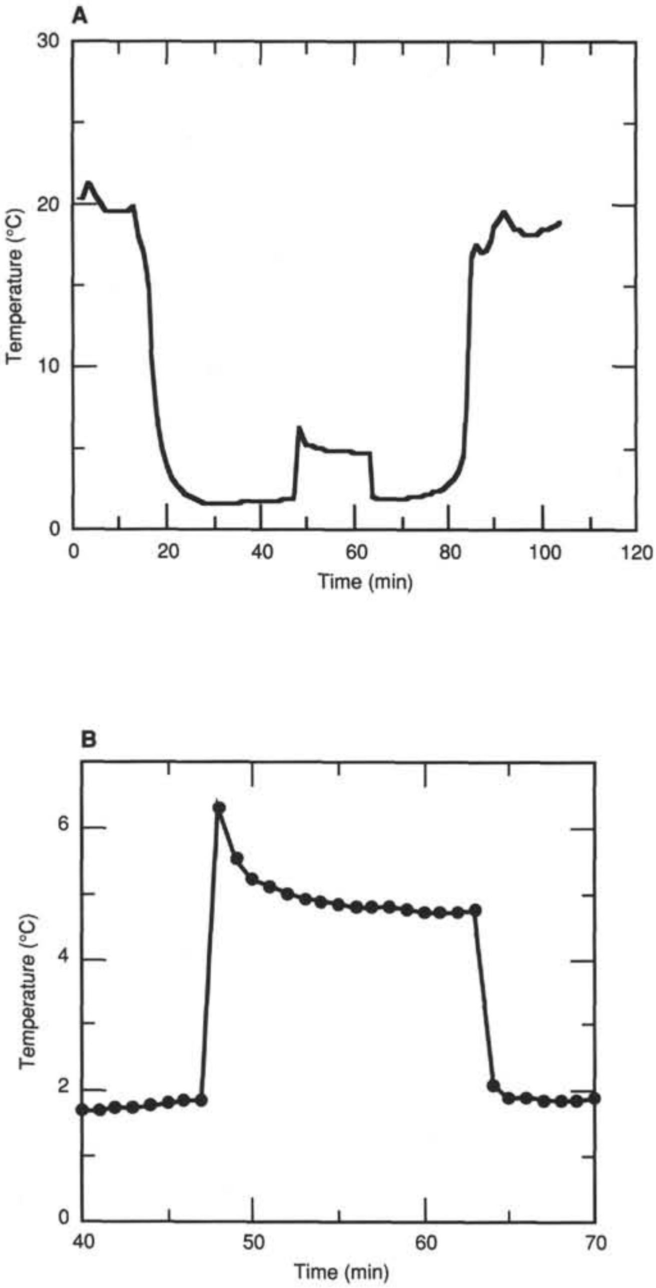

Figure 25. **A.** Temperature vs. time for Run 11R of the Barnes-Uyeda temperature tool at 107.1 mbsf in Hole 784A. **B.** An expanded plot showing the data when the tool was in the seafloor.

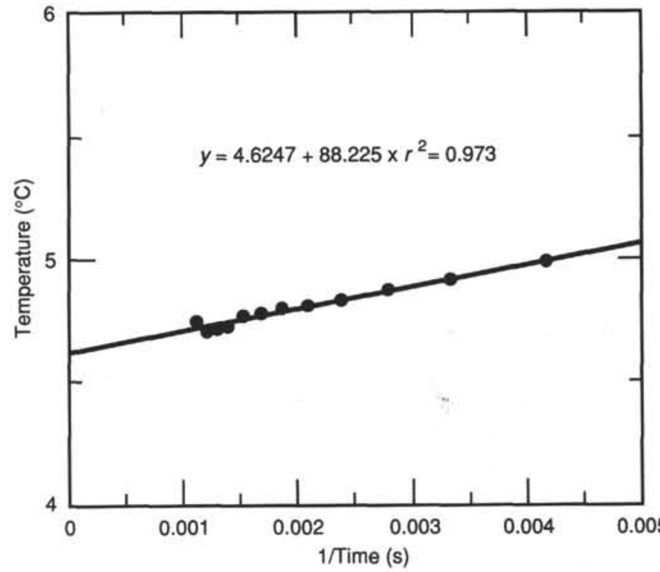

Figure 26. The corresponding reduced temperature fit for the second Barnes-Uyeda temperature run.

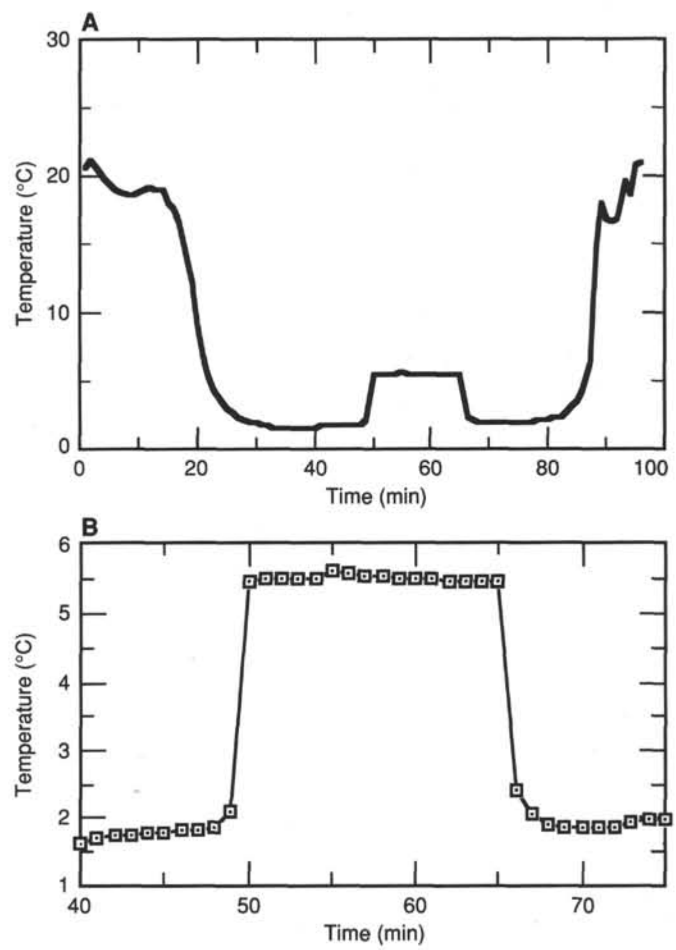

Figure 27. **A.** Temperature vs. time for Run 17R of the Barnes-Uyeda temperature tool at 145.6 mbsf in Hole 784A. **B.** An expanded plot showing the data when the tool was in the seafloor.

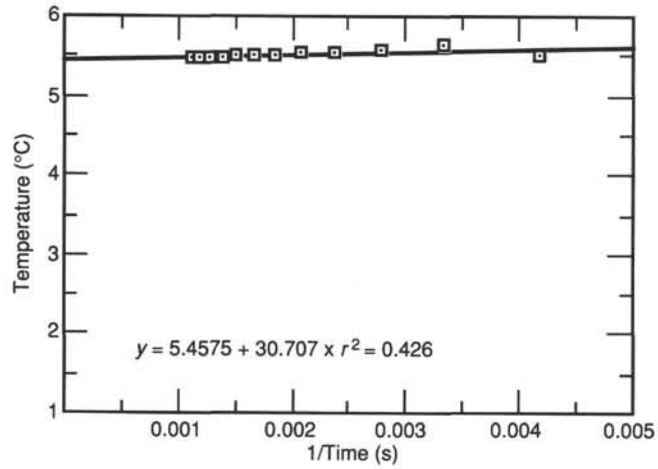

Figure 28. The corresponding reduced temperature fit for the third Barnes-Uyeda temperature run.

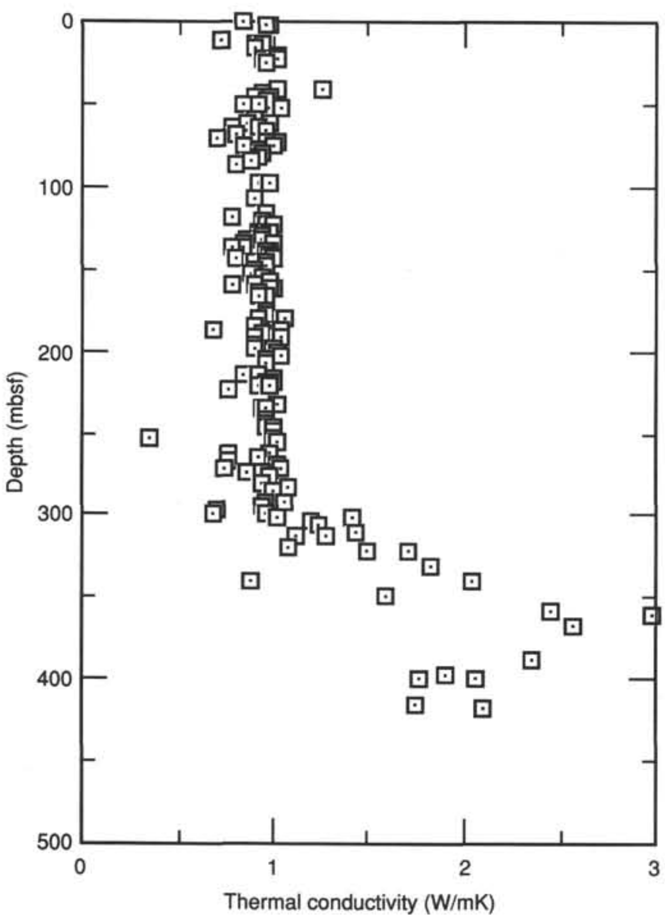

Figure 29. Thermal-conductivity results plotted vs. depth for Hole 784A.

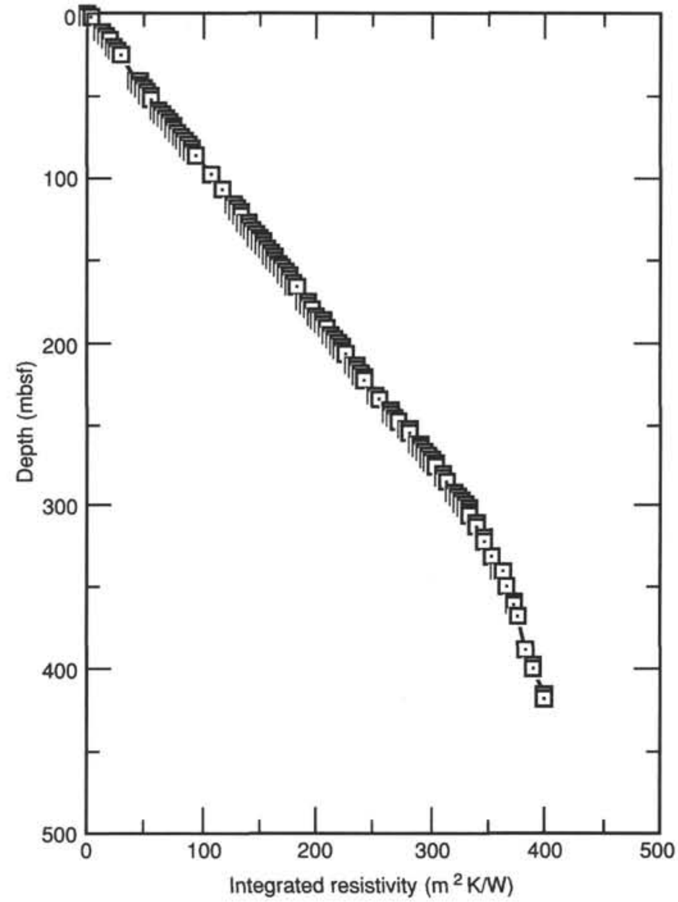

Figure 30. Integrated thermal resistivity and the depth integral of thermal resistivity plotted vs. depth for Hole 784A.

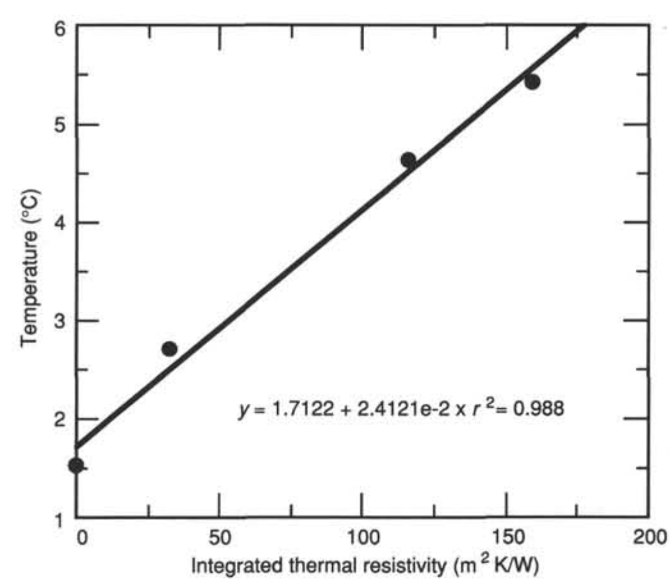

Figure 31. Temperature vs. integrated thermal resistivity for Hole 784A. The slope of the best-fitting linear regression is a heat-flow value of 24 mW/m^2.

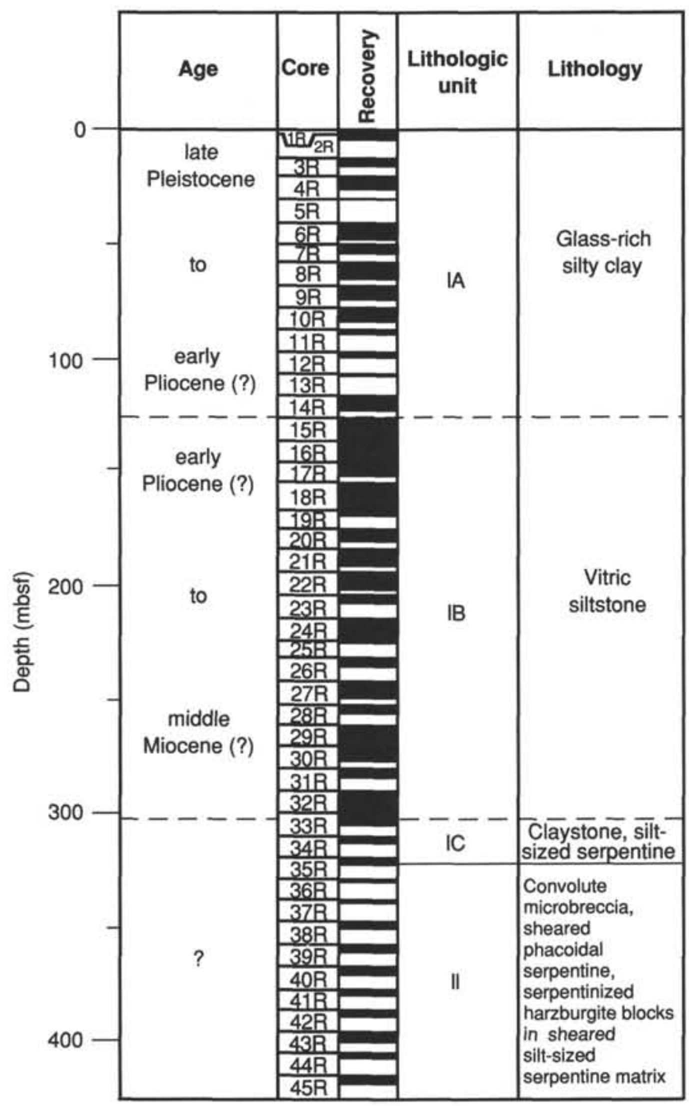

Figure 32. Core recovery and lithologic summary, Hole 784A.